MASTER IN ASTROPHYSICS AND SPACE SCIENCE

Erasmus Mundus Master
in Astrophysics and Space Science

Master Thesis

Close supermassive binary black holes and expected broad line shapes in active galaxies

Supervisors

Prof. Luka Popovic
Astronomical Observatory Belgrade

Prof. Francesco Tombesi
Astronomy Dept., University of Rome Tor Vergata

Prof. Dragana Ilic
Astronomy Dept., University of Belgrade

Author

Aurellio Deandra

Academic Year 2023/2024

TOR VERGATA UNIVERSITÀ DEGLI STUDI DI ROMA
UNIVERSITY OF BELGRADE
University of Bremen
UNIVERSITÉ CÔTE D'AZUR
Funded by the European Union

UNIVERZITET U BEOGRADU
MATEMATIČKI FAKULTET

Aurellio Deandra

CLOSE SUPERMASSIVE BINARY BLACK HOLES AND EXPECTED BROAD LINE SHAPES IN ACTIVE GALAXIES

Master's Thesis

Beograd, 2024.

Mentor:

dr Luka Popović
Astronomska Opservatorija, Beograd

Thesis Comittee:

dr Andjelka Kovačević,
Univerzitet u Beogradu, Matematički fakultet

dr Francesco Tombesi
Università degli Studi di Roma "Tor Vergata"

dr Dragana Ilić,
Univerzitet u Beogradu, Matematički fakultet

Date of Defense: _____

Ketika kita balikan cara pandang kita, kenyataan pun berubah.
(When we change our perspective, reality changes.)

- Dee Lestari

For you, who are waiting at home,
and you, who I will leave behind,

let us meet again, even if only for a moment.

This Master thesis is submitted in partial fulfillment of the requirements for the degree MASTER ASTROFIZICAR as part of a multiple degree awarded in the framework of the Erasmus Mundus Joint Master in Astrophysics and Space Science -- MASS jointly delivered by a Consortium of four Universities: Tor Vergata University of Rome, University of Belgrade, University of Bremen, and Université Cote d'Azur, regulated by the MASS Consortium Agreement and funded by the EU under the call ERASMUS-EDU-2021-PEX-EMJM-MOB.

Abstract

Sub-parsec supermassive binary black holes (SMBBHs) systems occur as the last stage before the merger of their component black holes. These SMBBHs systems are expected to have activity similar the one exhibited by active galactic nuclei (AGNs). PoSKI spectroscopic model shows that SMBBH have peculiarities in the broad Hβ lines compared to ordinary AGNs profiles. The model also shows that different component mass, mass ratio, and separation configuration, in addition to the positional configuration, gives different line profiles. In this thesis, candidates of sub-parsec SMBBH are picked from SDSS DR16 QSO catalogue. Using PCA method similar to the one performed by Eracleous et al. (2012), 270 objects with $z < 0.8$ and $SNR > 30$ are suspected to house SMBBH systems. Determination of mass, mass ratio, component separation, and positional configuration parameters are also performed with these objects, resulting in the highly confident parameters determination of 54 objects. Long-term observation of these objects will further confirm the existence of sub-parsec SMBBH, especially 24 objects that is determined to have component separation of 0.001 or 0.005 pc.

Keywords: line profile, principal component analysis, spectroscopy, supermassive binary black holes,

1. Introduction

1.1 Background

The merging of supermassive binary black hole (SMBBH) helps in the understanding of galaxy formation and evolution (Wang et al., 2023; Krolik et al., 2019). Since most galaxies host a supermassive black hole in its nucleus, SMBBH system should be expected when galaxies merge if the supermassive black hole is formed before the merger (Krolik et al., 2019). In addition, SMBBH merging is a source of low-frequency gravitational waves (Wang et al., 2023).

Various stage of supermassive black hole merger might aid the understanding of galaxy growth (Krolik et al., 2019). Kiloparsec-scale SMBBH have been studied quite rigorously with several examples of kiloparsec SMBBH (see for example Liu et al., 2018). The decaying or bit of these kiloparsec SMBBHs result in the formation of SMBBH systems with separation less than 0.1 pc (Begelman et al., 1980; Wang et al., 2023) surrounded by local gas and stars, known as the sub-parsec phase (henceforth will be referred to as sub-parsec SMBBH) (Popović et al., 2021). These sub-parsec SMBBH are the potential source of gravitational wave due further orbit decay caused by the emission of gravitational waves (Begelman et al., 1980). In addition, Krolik et al. (2019) noted that gravitational waves from SMBBH merger is observable only in a short timescale of around 10^3 s. With this small window of observation, there's a good chance that the observation is completely missed. Therefore, to ensure sufficient data, many SMBBH is needed, or at the very least, SMBBH candidates.

Compared to kiloparsec SMBBH system, sub-parsec SMBBH system are difficult to observe. High-resolution radio telescope has potential to detect SMBBH system in kiloparsec scale (Fu et al., 2011; Burke-Spolaor, 2011). Although direct observation of sub-parsec SMBBH is very difficult to implement using present-day equipment, indirect observation through how the SMBBH system affects its surroundings local gas and stars is plausible. The sub-parsec SMBBH system's orbital motion is reflected in the spectral characteristics. Therefore, one possible method of detection is using the peculiarity in the detected spectra (Popović et al., 2021, Wang et al., 2023). Using such method, the spectroscopic searches have identified around 100 SMBHH candidates (Eracleous et al., 2012; Nguyen, 2020).

The activity produced by the sub-parsec SMBBH is similar to the one observed in an active galactic nucleus (AGN) (Popović, 2012; Popović et al., 2021, Nguyen et al., 2020). Popović (2012) notes that AGN activity can be triggered by supermassive black hole merger is not a new idea. Hence, it is more accurate to label these SMBBH objects found by this method a "SMBBH candidates." Simulation modelling can be done to improve the confidence that these objects are SMBBH. The simulation is focused on finding the mass magnitude and the mass ratio of the SMBBH, in addition to the mean separation of the SMBBH. The orbital period can also be determined by extension and will also be determined using the modelling.

1.2 Scope and Aim

With the explained background, this master's thesis aims to determine whether it is possible to detect sub-parsec SMBBH using the spectral properties, particularly the shape of the spectral lines and the monitored spectral variability. To achieve this goal, a list of sub-parsec SMBBH candidates is needed, along with the means to verify these candidates.

Eracleous et al. (2012) did a sub-parsec SMBBH search using spectral properties using SDSS DR7 data for $z < 0.7$. Eracleous' search looks for peculiarity in the Hβ line, around the rest frame of 4290-5400 Å. The search results in 88 SMBBH candidates. Since then, SDSS have several updates, mainly the new BOSS spectrograph. The extended maximum observing wavelength for the spectrograph allows for the search to be broadened. In addition, Lyke et al. (2020) released a QSO objects catalogue based on SDSS DR16 data. Thus, the SMBBH candidates must be updated to account for the updates related to the SDSS.

To further refine the SMBBH candidates, a simulation modelling is be done. With the simulation that assumes PoSKI model (Popović et al., 2021) model, broad Hβ spectra lines are generated. The generated broad lines are then fitted to the Hβ spectra lines from the previously obtained SMBBH candidates.

Therefore, this master's thesis has two goals that are derived from the main goal:

1. Updating the SMBBH candidates catalogue with the spectra data of SDSS DR16 and widening the search to $z < 0.8$;
2. Further verifying the SMBBH candidates by obtaining an estimate of mass, mass ratio, and component separation using PoSKI model (Popović et al., 2021) by line profile comparison in optical wavelength, focusing on Hβ broad line.

1.3 Methodology

Two main methods are employed in this master's thesis, literature review and python programming.

Literature study

Literature study is mainly composed of studying various papers about AGN and the PoSKI model, analyzing the theoretical basis of spectroscopic detection of sub-parsec SMBBH system. The result of the literature study will be reflected mainly in chapter 2.

Python Programming

Programming using Python 3 language is done for the following steps:

a. Initial search of the SMBBH candidate from SDSS DR16 QSO catalogue,
b. Spectra simulation of several possible configurations of sub-parsec SMBBH,
c. Fitting the SMBBH candidates obtained from step (a) with the simulated spectra generated from step (b).

Chapters 3, 4, and 5 of this thesis book discuss steps a, b, and c respectively. In addition, processes that take shorter runtime is run on local computer, while the more demanding processes that take longer runtime is run on the SUPERAST computer provided by the University of Belgrade (Kovačević et al., 2022).

1.4 Thesis Book Structure

This thesis book will be structed in 6 chapters. The summary of each chapter are as follows:

- Chapter 1 presents the background on this thesis that includes the goal of this research, while also briefly presenting the research methodology,
- Chapter 2 presents the relevant theory on sub-parsec SMBBH, as well as the plausibility of SMBBH detection with the spectra peculiarity,
- Chapter 3 shows the search of the SMBBH candidate from SDSS DR16 catalogue and discusses its method,
- Chapter 4 shows the simulated spectra of sub-parsec SMBBH using pre-provided simulation code,
- Chapter 5 shows the result of the fitting of SMBBH candidates. This chapter shows the possible parameters of SMBBH candidates with a good fit, while also discusses the objects with bad fits,

- Chapter 6 gives the conclusions and suggestions for this thesis.

In addition to the mentioned chapters with the conclusion and future studies at the end, the following appendices are included:

- Appendices A derives some of the error propagation that is used in this thesis
- Appendices B discusses the effect of scaling.
- Appendices C gives the result of the fitting parameters, in addition to the simulated spectra of objects with very high level of confidence to be used for long-term observations.

2. Sub-Parsec SMBBHs and How to Detect Them Spectroscopically

2.1. Supermassive Binary Black Holes

Every massive galaxy is expected to host a supermassive black hole (SMBH) in its (Kormendy & Richstone, 1995) with mass ranges from 10^6 to 10^9 solar masses (Shemmer et al., 2004; Walker et al., 2014; Zuo et al., 2015). These black holes are accompanied by the accretion disc, composed of matter from its surroundings that increases its mass over time (Savić et al., 2019; Mayer et al., 2010). These accretion disc allows the emission around an SMBH to be observed since the accreted mass is converted into high energy radiation (Dobbie et al., 2009).

The increase in mass of SMBH due to its accreting masses demonstrated that SMBH evolves over time. In addition to the accreting mass, one other way that SMBH evolves are through mergers with other SMBHs (Volonteri et al., 2003a,b). According to Volonteri et al. (2003a), mergers of pre-galactic black holes sink into the centre due to dynamical friction, creating a large halo in the process. Accretion of gas in the merger remnants allows these black holes to become galactic SMBH (Volonteri et al., 2003a). Galaxy mergers are expected to produce a supermassive binary black hole (SMBBH)

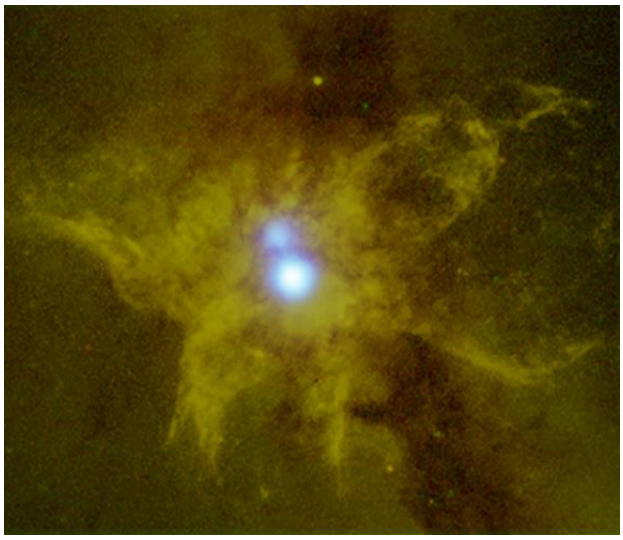

Figure II.1 An X-Ray image of NGC 6240 superimposed with an optical image available at. The blue X-Ray emission is showing two distinct emitters from the SMBBH. The image is available at: https://heasarc.gsfc.nasa.gov/docs/objects/heapow/archive/compact_objects/binary_bh_chandra.html (Credit: NASA/CXC/MPE/S.Komossa et al.)

system in the centre of the resulting remnant (Begelman et al., 1980; Roos, 1981). An example of this object is the NGC 6240 (see Figure II.1)**.**

SMBBH systems can be classified by the separation distance of the black hole component. Sub-parsec SMBBHs have separation distance smaller than 1 parsec, while the separation distance of a kiloparsec SMBBH is within 1000 parsec. The different classification of SMBBH shows the different stage of SMBBH system evolution.

Begelman et al. (1980) gives a standard picture of the SMBBH evolution. Dynamical friction due to distant stellar encounters decreases the separation distance of SMBBH, continued by the ejection of nearby stars through gravitational slingshot interaction when the orbital speed is comparable to the stellar velocity dispersion (Merrit & Milosavljević, 2005; Popović, 2012). The SMBBH orbit then decays, leading to the eventual merger of both black holes. (Popović, 2012; Savić et al., 2019; Begelman et al., 1980).

Gaseous dissipation seems to control the pairing process in SMBH mergers, especially for unequal-mass mergers which are expected to produce a SMBBH system with small separation distance (Kazantzidis, 2005). Collision-less process that is happening in a low-redshift, gas-poor galaxies (Kazantzidis, 2005), means that the SMBBH system can't transfer its angular momentum, but still undergoes mergers. In these systems, emission of gravitational wave is the cause of the orbit decay (Begelman et al., 1980). Therefore, SMBBHs one of the primary sources of gravitational waves, especially low-frequency gravitational waves (Popović et al., 2021; Wang et al., 2022). The merger of SMBBH itself emits a massive amount of energy in the form of gravitational wave, albeit at a very short timescale at around 10^3 s (Krolik et al., 2019).

2.2 Observing the SMBBH system

Due to their importance as a source of gravitational wave, SMBBH objects became objects of interest of observation. SMBBH systems with big separation of each components distance can be directly observed. A very active SMBBH system can be observed in short wavelength (see Figure II.1). Additionally, high-resolution radio observations can also be employed to perform direct imaging of SMBBH as demonstrated by the binary AGN confirmation by Fu et al. (2011) and Burke-Spolaor (2011). Fu et al. (2011) confirmed SDSS J150243.1+111557 to be a binary AGN with 7.4 kpc separation using Expanded Very Large Array, while Burke-Spolaor (2011) confirmed 4C +37.11 to have a component separation of 2.5 kpc using archival Very Long Baseline Interferometry.

However, sub-pc SMBBH is very difficult to directly observe. A SMBBH system can emit a spectrum that resembles one emitted by an active galactic nucleus (AGN) (Popović, 2012). While this fact gives a possible method of sub-parsec SMBBH observation, it might be difficult to differentiate sub-parsec SMBBH spectra to another AGN spectra.

According to the unified model of AGNs, the following components are present in most AGNs (Netzer, 2015):

- Accretion disc
- Broad line region (BLR) which consists of high-density, dust-free gas clouds with distance around 0.01 to 0.1 parsec from the black hole
- Central torus which is a dusty structure with dimensions of 0.1 to 10 parsec
- Narrow line region (NLR) which consists of dusty ionized gas with lower density and velocity extending form the torus to up to thousands of parsecs along the torus opening
- Thin molecular maser disk with similar size as the torus
- Gamma-ray emitting jet

Figure II.2 shows an illustration of unified AGN model without showing the maser disc and the jet. As stated before, SMBBH systems can emit an AGN-like spectra with evidence of Narrow Line Region (NLR), dusty torus, X-ray to infrared emission of accretion flow, and a Broad Line Region (BLR).

In a typical AGN emission, the emission from BLR dominates the line emission (Gaskell, 2008; 2009). According to Gaskell (2009) the BLR is a region in SMBH where

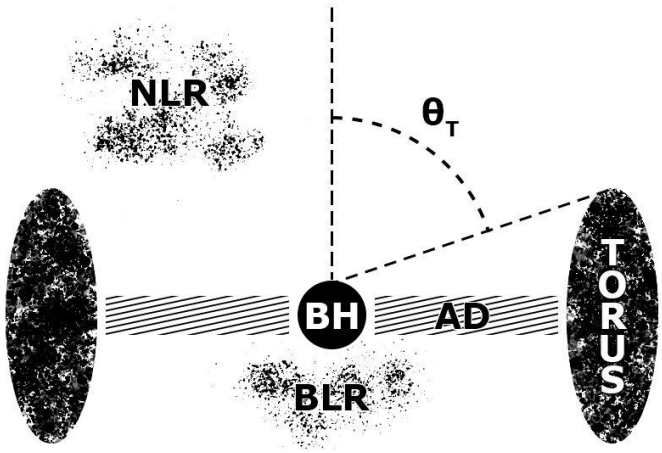

Figure II.2 A sketch of unified model of an AGN with the labelled black hole (BH), accretion disc (AD), narrow line and broad line region, the torus, and the covering angle. (Credit: Giuliani et al., 2021)

interstellar material that formed the thick torus gets evaporated. The BLR consists of the optically thin material while the optically thick material produces the continuum emission (Gaskell, 2009).

According to two-component model of AGN (Popović et al., 2004), the complex broad Hβ and Hα lines can be described with more than one gaussian profile, with a central broad component of low velocity. Some spectra that have a highly shifted broad component indicate an existence of accretion disc (Popović et al., 2004). Peculiarity in this highly shifted line may serve as a hint that an AGN spectrum emanates from a SMBBH system, since SMBBH system should have two accretion discs, one for each black hole component.

2.3 Spectroscopic model of sub-parsec SMBBH

AGNs that host an SMBH with an accretion disc will have its gas in the BLR ionized by the continuum emission (Popović et al., 2021). The BLR itself is optically thin (Gaskell, 2009), making the effect of radiative transfer is negligible. Here, SMBBH system as described in Popović et al. (2021), henceforth will be referred to as PoSKI model, is adopted due to it being the most recent general model of SMBBH (compare with object-specific model such as Volvach et al. (2023) model for 3C 273). In addition, PoSKI model gives an emphasis on the changes in spectra due to variation in mass and distance clearly, especially on the optical (Hβ) range, the wavelength of focus in this thesis.

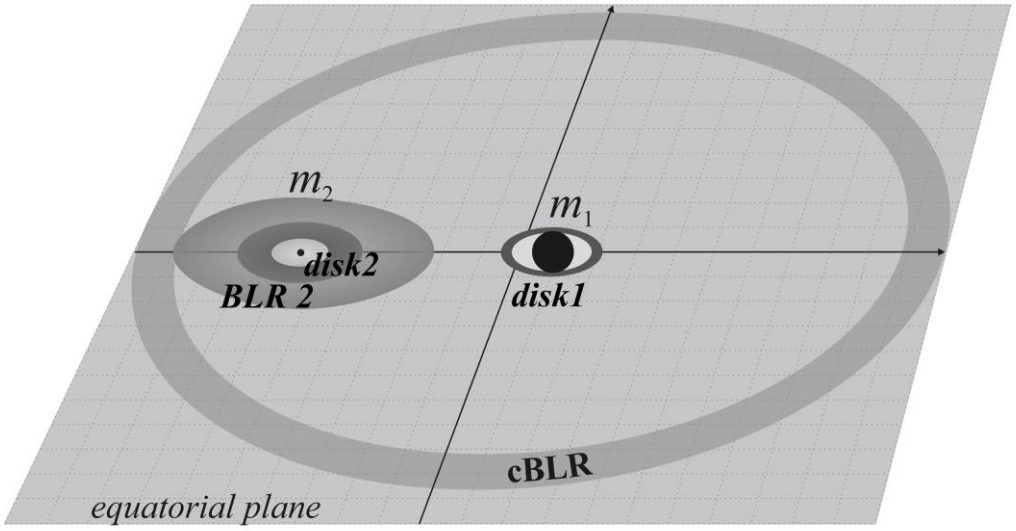

Figure II.3 An illustration of the SMBBH model, showing BLR from the less massive component, and a circumbinary BLR (cBLR). (Credit: Simic et al., 2016)

In PoSKI model, each of the SMBHs has their own accretion disc, in addition to a common circumbinary BLR (henceforth will be referred to as cBLR) (Popović et al., 2021). Figure II.3 shows an illustration of this model structure. However, cBLR might not be present in every SMBBH system and the following two cases are possible:

1. Continuum luminosity is too small to create cBLR and SMBH's BLRs are separated without contact.
2. Continuum luminosity creates a cBLR, which also means each SMBH's BLRs are inside the Roche lobes of each other.

For both cases, the following assumptions are considered (Popović et al., 2021):

1. The BLRs are flattened with the inclination similar to the accretion disc (Collin et al., 2006; Savić et al., 2019), making the BLR is in the same plane as the accretion disc.
2. Inner parts of the BLR overlaps with the accretion disc.
3. The BLR extends to a few light years in diameter, depending on the disc luminosity (Kaspi et al., 2005).
4. SMBH mass determines the Kinematics of the BLR (Peterson, 2014).

Every BLR (from each of the SMBHs and the cBLR) emits electromagnetic spectrum typical for an AGN (Popović et al., 2021). A simple dynamical PoSKI model shows how the interactions of each of the SMBHs accretion discs affecting the surface disc temperature. This change in surface temperature changes the line profile so that it differs from a typical AGN profile, and how certain difference in SMBBH system parameters affect how different the line profile is.

The subsections below adapt the spectroscopic PoSKI model in reverse, laying out the general equation for a line profile, then shows which of the SMBBH system parameters are affecting the changes in the profile according to PoSKI model with only dynamical shift considered. Further reading of Popović et al. (2021) is encouraged to fully understand how the equations are obtained from the SMBBH configuration.

2.3.1 Equation of BLR line profile.

Total BLR intensity can be written as:

$$I_{tot}(\lambda) = I_1(\lambda) + I_2(\lambda) + I_{cBLR}(\lambda) \qquad (II.1)$$

where $I_{cBLR}(\lambda) = 0$ for case where cBLR isn't created. Furthermore, each SMBH emits a Gaussian line profile:

$$I_i(\lambda) = I_i(\lambda_0)\exp\left[-\left(\frac{\lambda-\lambda_0\left(1+z^i_{dopp}\right)}{\sqrt{2}\sigma_i}\right)^2\right]\cos(i) \qquad (II.2)$$

and similarly, for the cBLR:

$$I_{cBLR}(\lambda) = I_{cBLR}(\lambda_0)\exp\left[-\left(\frac{\lambda-\lambda_0}{\sqrt{2}\sigma_{cBLR}}\right)^2\right]\cos(i) \qquad (II.3)$$

where λ_0 is the wavelength for H-beta where $\lambda_{H\beta} = 4861$ Å. Subscript i denotes the component while i in the equation denotes orbital inclination.

2.3.2 Broad line peak shift

Radial velocity of the SMBH components describe the peak shift of spectra lines from the transition wavelength of Hβ $\lambda_{H\beta}$. In Figure II.4, a visual illustration of this change is given. In equation (II. 2), z^i_{dopp} describes the Doppler correction for radial velocity v_i where $z^i_{dopp} = v_i/c$. To calculate the radial velocity, consider a binary system with arbitrary masses $m_{1,2}$ where the ratio of each component $q = m_1/m_2$ with $m_1 < m_2$. Period of a 2-component system with elliptical orbit with eccentricity e_{cc} (Hilditch 2001):

$$P^2 = \frac{4\pi^2 a^3}{G(m_1+m_2)}$$

where a is mean distance between component and G is gravitational constant. In the case of SMBBH, orbital period in years:

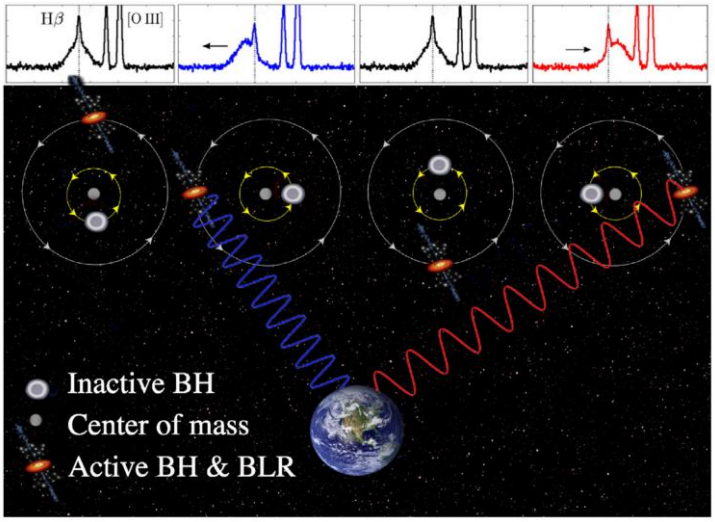

Figure II.4 Illustration of how radial velocity affect the peak shift of spectra lines. (Credit: Guo et al., 2019)

$$P_{orb} = 210\left(\frac{a}{0.1\,pc}\right)^{\frac{3}{2}}\left(\frac{2\times 10^8 M_\odot}{m_1+m_2}\right)^{\frac{1}{2}} \quad (II.4)$$

where $m_{1,2}$ is in $10^8 M_\odot$ unit. Mean anomaly, as introduced by Popović et al. (2021) with time variable t, initial moment of measurement τ, and orbital phase ϕ, is as follows:

$$M = \frac{2\pi}{P_{orb}}(t-\tau) = 2\pi\phi$$

Using the mean anomaly, Kepler's equation can be written in the form of:

$$M = E - e_{cc}\sin(E)$$

Extracting the eccentric anomaly E, true anomaly can be computed as:

$$\theta = 2\arctan\left(\sqrt{\frac{1+e_{cc}}{1-e_{cc}}}\tan\left(\frac{E}{2}\right)\right) \quad (II.5)$$

Radial velocity can then be computed in the observer frame as:

$$v_i(\theta) = K_i[\cos(\theta+\omega) + e_{cc}\cos(\omega)] + \gamma \quad (II.6)$$

with

$$K_i = \frac{2\pi a_i \sin(i)}{P_{orb}\sqrt{1-e_{cc}^2}} \quad (II.7)$$

where ω is arbitrary perihelion argument and γ is systemic velocity. In addition, $a = a_1 + a_2$. In PoSKI model, the following values are chosen: $\omega = 0^o$ while $\gamma = 0$.

It is demonstrated that shift in broad line peak is affected by the mean distance and mass of SMBBH system where, roughly $v_i \propto a^{-1/2} m_i^{1/2}$. In addition, mass ratio affects the radial velocity of each SMBHs as follows:

$$a_1 = \frac{qa}{1+q} \qquad a_2 = \frac{a}{1+q}$$

Since q assumes that $m_1 < m_2$, this shows that $a_1 < a_2$. With the established relation between radial velocity and distance, this shows that SMBH component that has smaller mass will show a larger peak shift than the more massive component. Additionally, eccentricity also shows an effect to the shift, albeit less significant than mean distance and mass. From equation II.6 and II.7, $v_i \propto e_{cc}/\sqrt{1-e_{cc}^2}$. This shows that a larger shift is expected with large orbital eccentricity.

2.3.3 Peak of composite line profile

Maximal intensity of the broad line at $\lambda_0 = \lambda_{H\beta}$ can be calculated as:

$$I_i(\lambda_{H\beta}) = \frac{\lambda L(H\beta)}{\sqrt{2\pi}\sigma_i} \tag{II.8}$$

Since $H\beta$ emission is within visual spectral range, thermal emission is the primary radiation mechanism. Temperature at the part that's not close to the central SMBH follows $T_{eff} \propto R^{-\beta}$ relation with the black hole radius. Assuming a standard disc model, $\beta = 3/4$. However, this only applies to a single SMBH system. In the case of SMBBH system the interaction between two black holes causes gravitational perturbations in the accretion disc. Matter flow also affects the system by introducing changes in accretion rate. Both are time-dependent effects due to changes in the distance between the black holes in the system as period progresses. With these changes, effective temperature becomes (see appendices A and B on Popović et al. (2021) for the in-depth derivation):

$$T^i_{eff}(t) = T^i_0 \left(1 + \frac{m_j}{m_i}\frac{R\cos(\beta)}{r_j(t)}\right)^{\frac{1}{4}} \left(\frac{f^i_E(t)}{f^i_{E,0}}\right)^{\frac{1}{4}} \tag{II.9}$$

where T^i_0 is the effective temperature for non-perturbed disc, f^i_E is the Eddington ratio of i-th component where $f^i_E = m_{acc,i}/m_{edd,i}$, and $r_j(t)$ refers to the distance between the perturbed disc of i-th component to the perturbing j-th black hole that can be written as follows:

$$r_j(t) = a(t) + \sqrt{1 + \left(\frac{R_i}{a(t)}\right)^2 - 2\frac{R_i}{a(t)}\cos(\phi)} \tag{II.10}$$

where $a(t)$ is the distance between the two SMBHs and ϕ is the angle between $a(t)$ and R_i observed from the centre of i-th component.

With this assumption, the radiated power emitted by a small ring-like element of the disc surface $dS = 2\pi r dr$ at distance r from the system centre is given as (Poindexter et al., 2008):

$$dL_i(t) = 4\pi\frac{2hc^2}{\lambda^5}\frac{dS\cos(i)}{\exp\left(\frac{hc}{\lambda k_B T^i_{eff}(t)}\right) - 1} \tag{II.11}$$

where h, c, k_B are Planck constant, speed of light, and Boltzmann constant. Integration of equation II.11 over entire disc surface gives the total luminosity as:

$$L_i(\lambda, t) \propto \int_{R_i^{in}}^{R_i^{out}} \lambda dL_i(\lambda, T_{eff}, t) \tag{II.12}$$

Since luminosity of the SMBBH system is determined by both SMBHs, meaning that $dL_{tot} = dL_1 + dL_2$ and equation II.11 becomes:

$$dL_{tot}(t) = 4\pi \frac{2hc^2}{\lambda^5} \left[\sum_{n=1,2} \frac{dS \cos(i_n)}{\exp\left(\frac{hc}{\lambda k_B T_{eff}^n(t)}\right) - 1} \right] \quad (II.13)$$

equation II.12 becomes:

$$L_{tot}(\lambda, t) \propto \int_{R_i^{in}}^{R_i^{out}} \lambda dL_{tot}(\lambda, T_{eff}, t) \quad (II.14)$$

Focusing on optical emission, inner disc radius R_i^{in} can be adopted as $R_i^{in} \sim 10\ R_g$. For the outer radius R_i^{out}, the following relationship is used (Vicente et al., 2014) assuming a Shakura-Sunayev accretion disc (Shakura & Sunyaev, 1973):

$$R_i^{out} = \frac{1}{2} r_0 \left[\frac{m_i}{10^9}\right]^{\frac{2}{3}} \quad (II.15)$$

The outer radius is given in light-days unit, while the SMBBH mass component is given in $M_\odot$. In addition, r_0 is assumed to be $4.5^{+0.7}_{-1.6}\ ld$.

2.3.4 Broad lines width

Since equation (II.2) and equation (II.3) shows a gaussian profile, the width is determined by the velocity dispersion σ_i. It is important to also note that velocity dispersion also determines the maximum intensity as shown in equation (II.8). Velocity dispersion σ_i is related to the BLR velocity for i-th SMBH component $v_{BLR}(m_i)$ as:

$$\sigma_i = \lambda_{H\beta} \frac{v_{BLR}(m_i)}{c} \quad (II.16)$$

With the assumption of BLR virialization,

$$v_{BLR}(m_i) = \sqrt{\frac{G m_i}{f_v R_{BLR}}} \quad (II.17)$$

where f_v is the virialization factor that, with the assumption of BLR virialization, $f_v = 1/\sin^2(i)$ (Afanasiev et al., 2019). For the case of cBLR, $m_{cBLR} = m_1 + m_2$. BLR size R_{BLR} can be estimated with the following relationship (Kaspi et al., 2005; Wu et al., 2004):

$$R_{BLR}^i \propto [\lambda L_i(\lambda_0)]^{0.69 \pm 0.05}$$

where $\lambda L(\lambda_0)$ is the luminosity at λ_0. With relation to equation II.12, it is shown that R_{BLR} changes over time according to the period completion of the SMBBH system. For the case of cBLR, the total luminosity is considered (see equation II.14).

3. Searching for Sub-Parsec SMBBH from SDSS QSO Catalogue

As described previously in chapter 2, broad emission lines are present in AGN that host single SMBH. These complex emission lines can be described with two-component model (Popović et al., 2004; Bon et al., 2009; Rakić, 2022). However, line profile of some of these AGNs are unusual which may indicate extremely complex BLR emission, indicating presence of SMBBH system. Section 2.1.2 shows that using PoSKI model, SMBBH causes spectra peculiarities in the BLR region, mainly the shift and asymmetry (see section 2.1.2.2). Previous study by Eracleous et al. (2012) catalogued 88 of such objects and classified them as SMBBH candidates.

One of the goals of this thesis is to find the good candidate of SMBBH by updating previous search result by Eracleous et al. (2012) in addition to widening the search. This chapter described the first step to determine SMBBH candidates from SDSS DR16 QSO catalogue, which is the object selection step. PCA method is employed to semi-automatically determine possible SMBBH candidates. This selection step largely follows the one described in Eracleous et al. (2012) and Boroson & Lauer (2010).

3.1 Selecting and preprocessing of spectra

Spectra analysis is done on the optical wavelength, focusing on the Hβ region. Wavelength range of 4000 – 5700 Angstrom as described by Boroson & Lauer (2010) is employed. The choosing of this wavelength range is somewhat arbitrary but will prove useful during spectra subtraction that is described in section 5.1. Considering the upper limit of the wavelength range, the search is focused on low redshift objects.

Using older SDSS DR7 QSO, Eracleous et al. (2012) used objects with redshift $z < 0.7$. However, SDSS DR16 QSO catalogue (Lyke et al., 2020) is used in this thesis. As of writing, the most recent SDSS data release is SDSS DR18 (Almeida et al., 2023), but the SDSS DR16 is still the most recent QSO catalogue with spectroscopically confirmed quasi-stellar objects. It should be noted that SDSS instrument received an upgrade prior to releasing the DR16 QSO catalogue, with the upgrade of interest being the BOSS spectrograph in 2009 that upgrades the upper observing wavelength limit from 9100 angstrom to 10400 angstrom (Smee et al., 2013). This allows for selection of objects with

the highest redshift being $z{\sim}0.82$. In practice, 76466 objects with $z < 0.8$ were chosen instead. This is done to exclude the objects that are too close to the upper wavelength limit that may have bad SNR.

Eracleous et al. (2012) compiles 88 SMBBH candidates out of around 15900 objects. With the newer catalogue and a wider redshift filter, detection of more objects is expected. Arbitrarily assuming the same percentage of detection, ~ 420 objects should be classified as SMBBH candidates. This number includes new SMBBH candidates, as well as objects previously classified by Eracleous et al. (2012).

All spectra are preprocessed using FANTASY package (Ilić et al., 2020; Rakić, 2022; Ilić et al., 2023)[1]. The first goal of this preprocessing is to shift the observed wavelength into rest wavelength, while the second goal is to deredden the spectra to account for interstellar extinction (Fitzpatrick, 1999). This ensures a more accurate analysis, especially when doing the fitting.

3.2 Searching spectra peculiarities with PCA

Principal component analysis (PCA) is employed to find unusual broad line profiles which may indicate presence of SMBBH in the center of AGNs. PCA method used is described in Boroson & Lauer (2010) and Eracleous et al. (2012), where eigenspectra are extracted from a subset of objects as the sample. Several eigenspectra are then used to reconstruct the object spectra. Result from Eracleous et al. (2012) suggests that sub-parsec SMBBH system are the outlier objects. Therefore, it is expected that SMBBH spectra should have a poor reconstruction using the first few eigenspectra, indicating peculiarities that weren't expressed in these first few eigenspectra.

3.2.1 Principal component analysis

Principal component analysis (PCA) is a technique for reducing data dimensionality to interpret large dataset easier, while also preserving as much statistical information as possible (Jolliffe & Cadima, 2016). In practice, PCA reduces the dataset into principal components that are linear functions to the original dataset (Jolliffe & Cadima, 2016). These principal components provide a descriptive look at the dataset.

Mathematically, PCA applies linear algebra methods to perform the dimensionality reduction, re-expressing the data as a linear combination of its basis vector (Shlens, 2014)

[1] FANTASY package is available on https://fantasy-agn.readthedocs.io/en/latest/index.html

(see also equation III.3). Rigorous mathematical description of PCA is not presented here, as the PCA process is done through a python package directly (see section 3.3.1). Shlens (2014) and Gewers et al. (2021) give a detailed and comprehensive mathematical view of PCA process. In any case, a quick step-by-step procedure of performing PCA are as follows (Shlens, 2014):

1. Organize data as $m \times n$ matrix, with m is the number of measurement types and n is the number of samples.
2. Perform mean subtraction for each measurement type.
3. Calculate the singular value decomposition (SVD) or the eigenvectors of the covariance.

Covariance measures the degree of linear relationship between two variables (Shlens, 2014). Additionally, SVD is used to find the solution of the following matrix equation (Shlens, 2014):

$$\boldsymbol{X} = \boldsymbol{U}\Sigma\mathbf{V}^{\mathrm{T}} \qquad (III.1)$$

with $\boldsymbol{X}$ is the data matrix, $\boldsymbol{U}$ and $\boldsymbol{V}$ are the vector matrix with size $n \times n$ and $m \times m$ respectively, and Σ is a diagonal $n \times m$ matrix filled with singular values. It is also important to note that the assumptions of performing PCA are as follows (Shlens, 2014):

- Data is assumed to be linear combination of its basis vector
- Assumption of high signal-to-noise ratio (SNR) of the data, and large variance is deemed important
- Orthogonality assumption of the principal component.

Previous literatures (i.e. Francis et al., 1992; Boroson & Lauer, 2010; Eracleous et al., 2010) employed PCA into spectra analysis of quasi-stellar objects (QSO). Performing PCA on a spectra dataset produces eigenspectra with diminishing eigenvalue, meaning that the first few eigenspectra describe the most common elements of the dataset. For analyzing QSO spectra, the following equation for SVD is used instead of equation (III.1), solving for matrix $\boldsymbol{V}$ (Boroson & Lauer, 2010):

$$\boldsymbol{V^T C V} = \Sigma \qquad (III.2)$$

In this equation, $\boldsymbol{C}$ is the cross-correlation matrix with size $n \times n$, representing cross product of each spectrum with each other. The columns of matrix $\boldsymbol{V}$ contains the eigenvector which is then transformed into eigenspectra by multiplying them with the input spectra, and the diagonals of Σ gives the eigenvalues, which is the expected variance of principal component (Vanderplas et al., 2012; Ivezić et al., 2014).

3.2.2 Automated filtering using Python

The `sklearn` python package allows a relatively simple way to perform PCA of the objects, including the calculation of SVD as shown in equation III.1 and III.2. However, all spectra need to have the same spectral resolution, which means that the number of points and position of wavelength must be equal. Every spectrum is rebinned to Boroson's wavelength range, with wavelength resolution of 1. The rebinning is done for the flux and error. Rebinning of error value for each wavelength point uses percent error value relative to the flux at that point[2]. This is done to better reflect how the same error value will have more significant impact on the smaller flux than larger flux. In addition, this is also done to avoid unrealistic jumps in interpolated absolute error.

The PCA documentation from `sklearn` suggests scaling the data before performing PCA. Previous spectra analysis with PCA (Francis et al. 1992) did not scale the flux, with the reason being that the PCA result is insensitive to scaling. Another reason of scaling not being performed is that the eigenspectra obtained does not conform to previous attempt of PCA (Boroson & Lauer 2010). Appendix B explores more about this scaling effect. Instead of feature scaling, normalization is performed. The normalization procedure follows that described by Francis et al. (1992) as follows:

1. Each spectrum is scaled to its own mean value
2. Mean spectrum is calculated as average flux in each wavelength from all spectra
3. Every spectrum is subtracted with the mean spectrum to reduce to 0 mean.

A different normalization procedure is also performed on the PCA result in order to make the sum of the values equal to 1.

After spectra rebinning and normalization, PCA is then performed. 1000 spectra with the highest SNR were chosen as PCA samples. Figure III.1 shows the first 4 eigenspectra obtained. Note that the first eigenspectrum has a similar shape with mean flux spectra, and thus, the first eigenspectrum component can be interpreted as mean component. The second eigenspectrum might shows error on the mean, but this interpretation is still open for further analysis. It's important to note that the third eigenspectrum shows an importance near the Hβ wavelength that differs from previous eigenspectra and the mean which shows more emphasis on the OIII lines. The interpretation of the third eigenspectra is that most spectra show strong OIII lines while others may show stronger Hβ line.

[2] Appendix A.1 presents a more accurate error propagation for interpolation. However, the more accurate propagation is not used in this step, with the main reasoning being that the manual filter done later (see section 3.2.3) should mitigate this inaccuracy so that the inaccurate error propagation can be reasonably ignored. The more accurate error propagation is still used in a later step (see section 5.1.2).

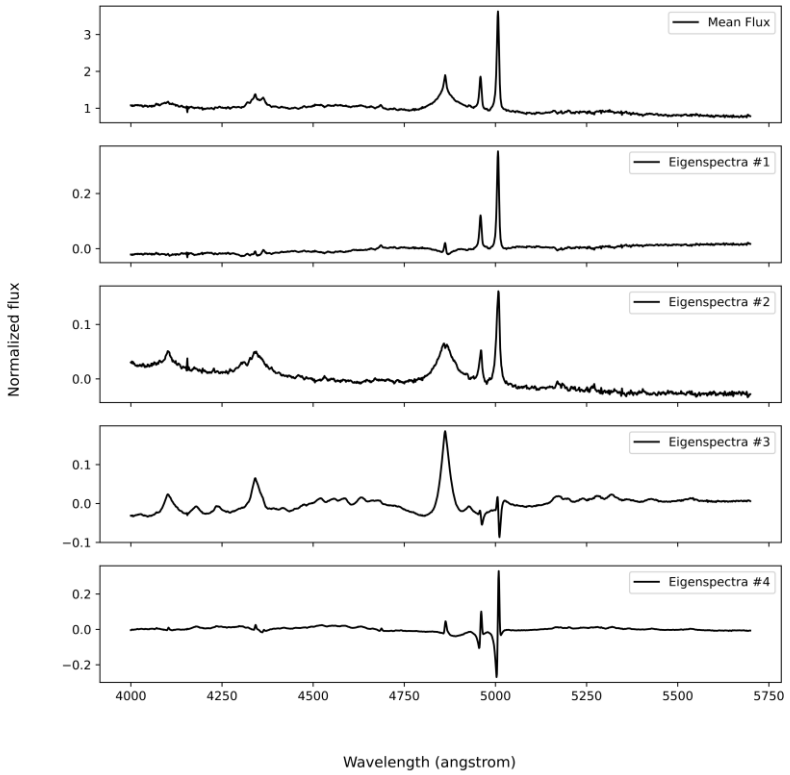

Figure III.1 The first 4 obtained eigenspectra as the result of the PCA process, in addition to the mean flux spectra.

Eracleous et al. (2012) uses only the 5 most significant eigenspectra to reconstruct the spectra, arguing that only the most common properties are reconstructed. Following that, only the first 5 eigenspectra, in addition to the mean value, is used in this thesis too. Expected obtained variance of reconstruction using 5 eigenspectra, expressed by the cumulative sum of the eigenvalue (Vanderplas et al., 2012; Ivezić et al., 2014), is 92%. This value is interpreted as 92% of the most common properties should be reconstructed. Figure III.2 shows that using more eigenspectra only gives a small increase in the expected obtained variance. In addition, using more eigenspectra also risks the less common parameters that may be associated with SMBBH system to be included in the reconstruction, leading to exclusion of objects that might have been SMBBH candidates.

Adapted from astroML (Vanderplas et al., 2012; Ivezić et al., 2014), reconstructed flux using the first 5 eigenspectra can be expressed with the following equation:

$$f_{recons.\lambda} = f_{mean,\lambda} + \sum_{i}^{5} (a_i \cdot e_{i,\lambda}) \qquad (III.3)$$

with coefficient a_i, defined as the corrected projection (Boroson & Lauer, 2010), are obtained for each eigenspectra e_i with the following:

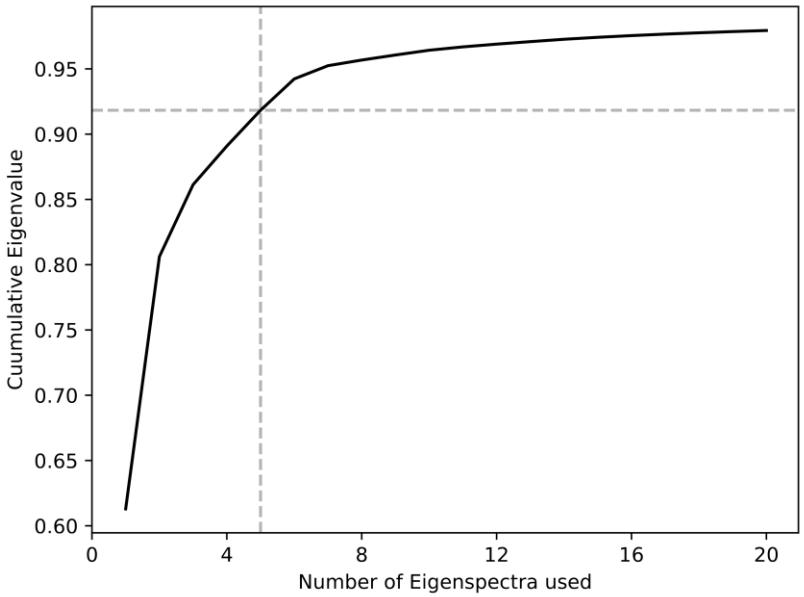

Figure III.2 Cumulative eigenvalue as representation of reconstruction accuracy. The faint dashed line shows the cumulative eigenvalue of using 5 eigenspectra to perform spectra reconstruction.

$$a_i = (e_{i,\lambda} \cdot f_{SDSS,\lambda} - f_{mean,\lambda})$$

Additionally, a reduced χ^2 parameters is used to quantify the goodness of fit. Adapted from Boroson & Lauer (2010),

$$\chi^2_{reduced} = \frac{\chi^2}{\nu} = \frac{1}{\nu}\left(\sum_{\lambda} \frac{f_{SDSS,\lambda} - f_{recons,\lambda}}{\sigma^2_{\lambda}}\right) \qquad (III.4)$$

where σ^2_{λ} denotes the observation error in the SDSS spectra, and ν denotes spectral pixels, i.e. the number of points within the wavelength range. Since the spectra are rebinned, the spectral resolution is the same. Figure III.3 shows two examples of the reconstruction of high SNR spectra, with one of them being the accepted SMBBH candidate, while the other is the rejected.

Initially, Eracleous et al. (2012) threshold for the goodness of fit $\chi^2/\nu > 3$ is chosen. However, this results in too many objects passed the filter and classified as an outlier. One of the possible causes of this is the inaccuracy of spectra reconstruction. Quick review of outlier spectra shows a high χ^2/ν value even with visually accurate reconstruction. While further analysis is needed to determine the exact cause of this issue, two workarounds are done to limit the number of objects analyzed. The first one is to limit the analyzed objects to only include objects with $SNR > 30$, meaning that only 1472 out of the 76466 objects will be analyzed. This condition is not ideal since 1000 of 1472 objects are included in the PCA sample and might introduce some bias. However,

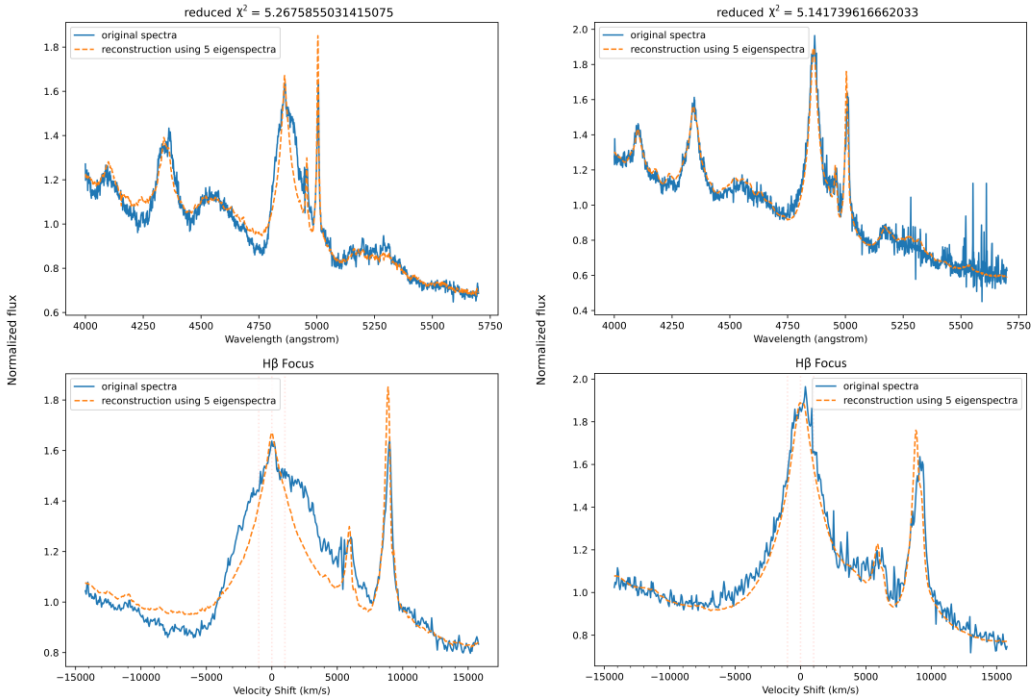

Figure III.3 Spectra of the SDSS 093728.57+324548.3 (*left*) and SDSS 215014.76-065314.4 (*right*). The whole 4000-5700 angstrom wavelength range is shown on top and +- 15000 km/s shift from H_beta wavelength (4861 angstrom) is shown on the bottom. On the bottom images, a faint dotted line is used to mark the +- 1000 km/s as one of the criteria of Eracleous object. The left object is accepted as SMBBH candidate, specifically the Eracleous object (evident of asymmetry and the >1000 km/s broad peak shift from its narrow line) while the right object is rejected as SMBBH candidate. Additionally, the reduced $\chi 2$ value is shown.

this is deemed an acceptable flaw since this helps cut the number of spectra analyzed for the manual filter, while a fix of the PCA process can be formulated for future studies.

The second workaround is to update the χ^2/ν threshold. To determine the updated threshold, the reconstruction is compared to objects classified as SMBBH candidate by Eracleous et al. (2012). Out of 88 SMBBH candidates, only 36 objects were available in the DR16 QSO catalogue. One confirmed cause of this is due to some of the objects have different designation that are off by 0.01 second in the RA and 0.1 second in the declination[3]. Other causes of this discrepancy might be due to inaccurate filtering or data corruption. Furthermore, only 28 out of 36 objects have $\chi^2/\nu > 3$, with 9 of them have $SNR > 30$. This reduced χ^2 value further shows small differences in method used by Eracleous et al. (2012) and this study. One idea to further refine this method is to do some form of normalization before calculating the χ^2/ν value. Flux can be normalized to constant mean value, or to normalize the flux to maximum flux in each spectrum.

[3] These objects are assumed to be the same object in section 5.2.3.

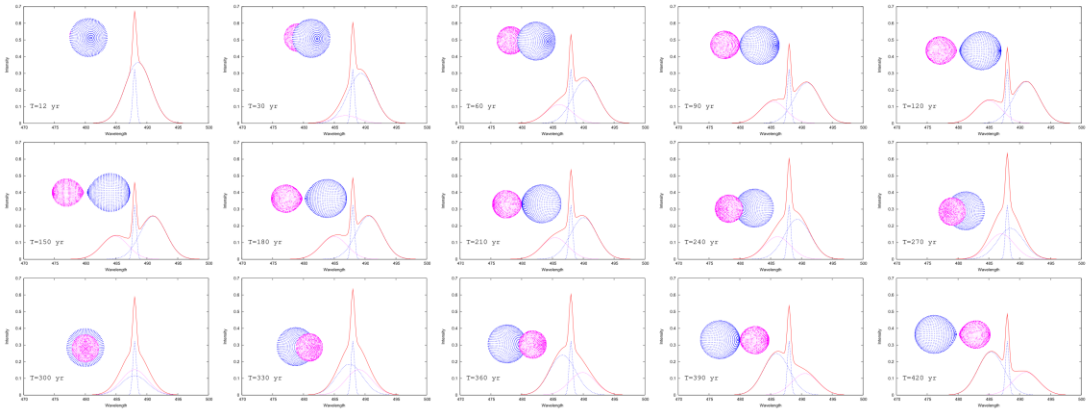

Figure III.4. Simulated spectra of SMBBH spectra with $m_1/m_2 = 0.5$ and distance $R = 0.1\ pc$ with earlier Popović (2012) model. In this simulation, the narrow Hβ is arbitrarily added. (Credit: Popović, 2012)

The result of this automatic filter is 752 objects that will be manually filtered, which means more than half of the objects are flagged as an outlier. Further viewing of some reconstructed spectra shows that although the reconstruction shows a visually good fit, they still show $\chi^2/\nu > 4.5$ (see Figure III.3 for example).

3.2.3 Manual (visual) filter and result

Spectra that passed the automatic filters are then analyzed visually. Eracleous et al. (2012) gave additional criteria to the visual filter. These criteria are as follows:

- Exclusion of objects with Hβ broad shift < 1000 km/s
- Exclusion of objects with shelves and inflection if the dominant broad peak at $v{\sim}0$
- Exclusion of objects with double peaks
- Retain objects with strong displaced peak
- Retain objects with extended wing near Hbeta narrow lines
- Retain flat-topped profiles if $v \neq 0$.

Objects that conform to the above criteria will henceforth be referred to as Eracleous objects.

Simulation using an older model (Popović, 2012) shows that depending on the position, SMBBH can show spectra that different from Eracleous objects' spectra (see Figure III.4), which is confirmed further with simulation using PoSKI model that will be explored in chapter 4. Objects exhibiting the following characteristics in the broad Hβ are passed, with the given example refer to the plotted spectra during period T in Figure III.4:

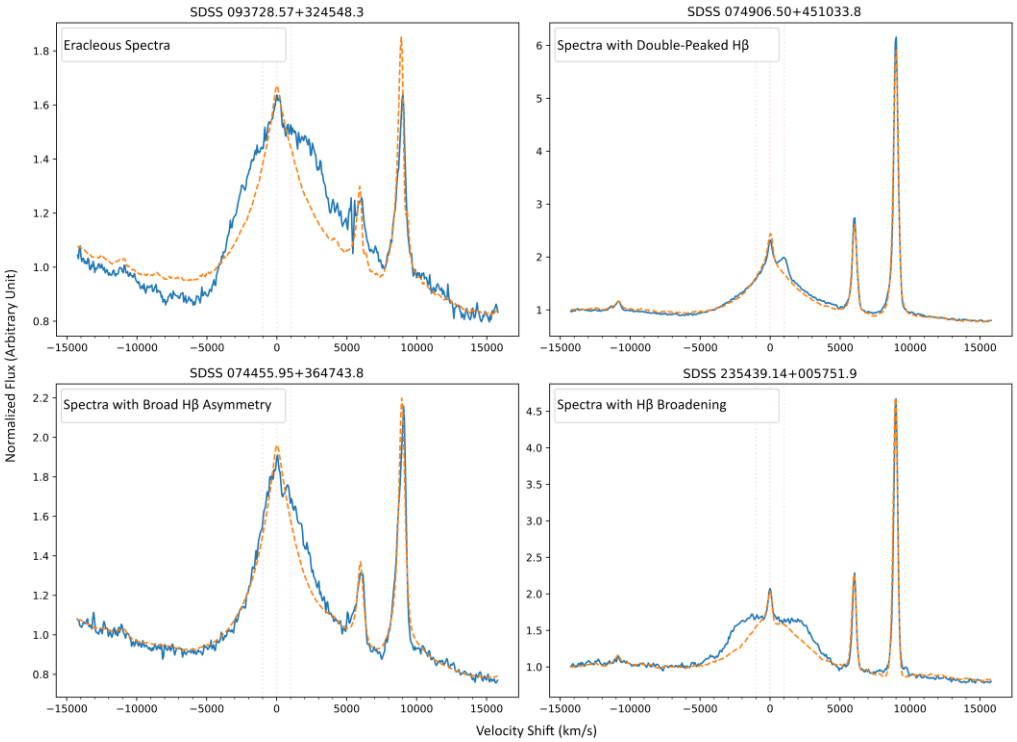

Figure III.5. Hβ focused spectra (similar to the bottom plots of Figure III.3) of 4 SDSS objects, showing the example of the object classified as Eracleous object (*top left*), double-peaked object (*top right*), asymmetry-only object (*bottom left*), and broad-only object (*bottom right*).

1. Double-peaked spectra (e.g. $T = 120\ yr$ and $T = 150\ yr$)
2. Signs of asymmetry (e.g. $T = 12\ yr$ and $30\ yr$)
3. Shows significant broadening. (e.g. $T = 300\ yr$)

Objects which spectra exhibit these characteristics are given lower priority than the Eracleous objects. Finally, the result of the manual filter is shown in table III.1, with the example of each classification of objects are shown in Figure III.5.

Table III.1. Number of objects for each classification

Object Classification	**Number of Objects**
Eracleous Objects	159
Double-peaked	29
Asymmetry Only	75
Broad Only	31
Total Objects	**294**

4. Modelling the Optical Spectra of Sub-Parsec SMBBH

Using PoSKI model discussed in section 2.3, several spectra is simulated. In this chapter, the simulation results are presented and discussed, highlighting the effect of several parameters, specifically mass of each component, mean separation of SMBBH components, and SMBBH period, to the Hβ BLR spectra. The simulation is done using Python code by Simić et al. (2024) with several modifications.

4.1 Simulating the spectra

The simulations are done with component mass M_i ranging from 10^6 to 10^9 $M_\odot$, with mass ratio of 1:1 and 1:2. This gives 8 mass configurations to simulate. Mean separation settings of $R = 0.001,\ 0.005,\ 0.01, 0.02$, and 0.1 parsec are also used for each mass configuration. It is assumed that the simulated spectra do not have any errors.

To account for time-dependent variations, 100 variations of time are used for each mass and mean separation configuration. This variation corresponds to the SMBBH position in which the spectra are simulated which ranges from 0% to 99% of the orbital period of the SMBBH with certain mass and mean separation configuration. In addition, to focus on Hβ wavelength, the wavelength range of 4500 to 5200 Å is used, which roughly corresponds to $\pm$ 20 000 km/s velocity shift from Hβ wavelength center.

Table IV.1 Constant parameters set for the simulation

Parameter	Set Value
Object inclination	45°
Orbit eccentricity	0.3
ω[1]	0
Number of full orbit	1
Number of evaluated time	100 points from 0 - 99% of full orbit
Roche emission ratio[2]	0.7
Wavelength Range	1000 points from 4200 - 5200 Å
Relativistic boosting[3]	0.7
Object Redshift[4]	0
Continuum wavelength[5]	5100 Å
Hβ wavelength	4861 Å

[1]See equation II.6
[2]Emission distribution over Roche BLR and cBLR, affecting cBLR contribution of emission
[3]Doppler beaming effect for continuum and BLR emission (see equation 21 in Popović et al (2021))
[4]This is set to 0 to evaluate the emission in rest wavelength
[5]Wavelength in which the continuum is evaluated

The total number of spectra simulated should be 400, one for each mass and mean separation configuration at a given period completion. Unfortunately, the simulation fails for some of the variation parameters due to program limitation. If the mean separation is set to 0.001, the simulation fails for $M_i = 10^9\ M_\odot$ for both mass ratio and $M_i = 10^8\ M_\odot$ for 1:2 mass ratio. The simulation also fails for $M_i = 10^9\ M_\odot$ with 1:2 mass ratio and mean SMBBH separation of 0.005. Therefore, only 360 spectra are successfully simulated and used.

To focus on the effect of SMBBH component mass and mean separation distance, several parameters in the simulations are kept as constant. Table IV.1 shows the input parameters that are set to constant.

Table IV.2 Orbital period for every simulated mass and separation configuration

Component Separation (pc)	Component Mass ($M_\odot$)	Mass Ratio	Orbital Period (Years)
0.001	10^6	1:1	2.058
		1:2	1.664
	10^7	1:1	0.663
		1:2	0.526
	10^8	1:1	0.206
0.005	10^6	1:1	22.782
		1:2	18.602
	10^7	1:1	7.204
		1:2	5.882
	10^8	1:1	2.302
		1:2	1.860
	10^9	1:1	0.782
0.01	10^6	1:1	65.090
		1:2	52.614
	10^7	1:1	20.377
		1:2	16.638
	10^8	1:1	6.508
		1:2	5.261
	10^9	1:1	2.058
		1:2	1.664
0.02	10^6	1:1	184.100
		1:2	150.318
	10^7	1:1	58.218
		1:2	47.059
	10^8	1:1	18.410
		1:2	14.881
	10^9	1:1	5.764
		1:2	4.706
0.1	10^6	1:1	2037.719
		1:2	1680.596
	10^7	1:1	644.383
		1:2	531.452
	10^8	1:1	203.772
		1:2	166.379
	10^9	1:1	64.438
		1:2	52.614

4.2 Simulation result

The following subsections discuss and show how component mass and separation affect simulated spectra using PoSKI model. Additionally, table IV.2 shows the orbital period of each of the component mass and separation configuration based on equation II.4.

4.2.1 Effect of component mass on spectra

Component mass and mass ratio seems to affect broad Hβ spectra line the most, affecting peak shift (see section 2.3.2), composite peak flux (see section 2.3.3, especially equation II.13 and II.14), and broad line width (see section 2.3.4, especially equation II.16). It is also shown that larger component mass causes said parameters to be larger. With a mass ratio of 1:1, it is expected to have a symmetrical spectrum with the symmetry line in the Hβ wavelength of 4861 Å, while other mass ratios (in this case 1:2) should give asymmetrical spectra. Figure IV.1 and IV.2 show the simulated spectra of the 8 mass configurations, highlighting how mass affect the spectra at pericenter position (50% of period) and at mean separation of 0.1 pc. Pericenter position is chosen to highlight the maximum shift caused by the radial velocity (see section 2.3.2).

It is clearly shown that SMBBH with larger component mass show a larger broad peak shift for each component, causing broadening of the total Hβ. With larger shift, the spectra will appear to have double peaks. In Figure IV.1 and IV.2, it seems that double peaks can only occur in very massive SMBBH. However, this double peak can occur in less massive SMBBH, provided the mean separation is small enough (see section 4.2.2).

Unequal SMBBH component mass, with ratio other than 1:1, results in spectra asymmetry. How asymmetric a spectrum is might suggest the mass ratio. The $10^9\ M_\odot$ simulation of 1:1 mass ratio in Figure IV.1 seems to have an asymmetry, where it's larger on the right side. However, this is deemed to be caused by limitation of the simulation code.

While a more quantitative measurement of FWHM can be done, it can be seen visually that each BLR component have a larger line width for a more massive system. The spectra detected by the instrument is the total Hβ spectra and it's difficult to parse each BLR component. Therefore, if a is broader-than-expected (see section 3.2.2 and 3.2.3), it may indicate a SMBBH system.

Absolute flux is value is shown in Figure IV.1 and IV.2, and it shows that more massive SMBBH system has a more intense emission. However, the line shapes are

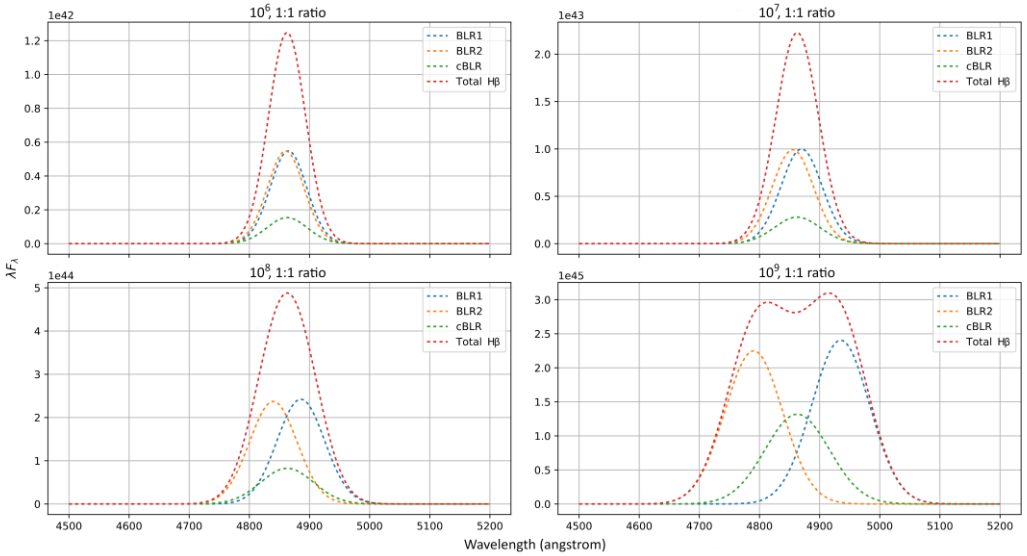

Figure IV.1 Simulated SMBBH flux to highlight the comparison of the effect of mass (shown in $M_\odot$ unit) at SMBBH separation of $R = 0.1$, while setting the mass ratio to be 1:1. The spectra are taken at 50% period completion (at pericentre position) of each configuration for maximum shift. Total Hβ refer to the total emission from the BLR of each component in addition to the circumbinary BLR. Note that the flux scale at each spectrum is different.

distinct enough for the variations in mass configuration (and subsequent variations). Due to this, simulated spectra are normalized so that the maximum flux has a value of 1. These normalized spectra are used in subsequent figures for simulated spectra and object spectra fitting.

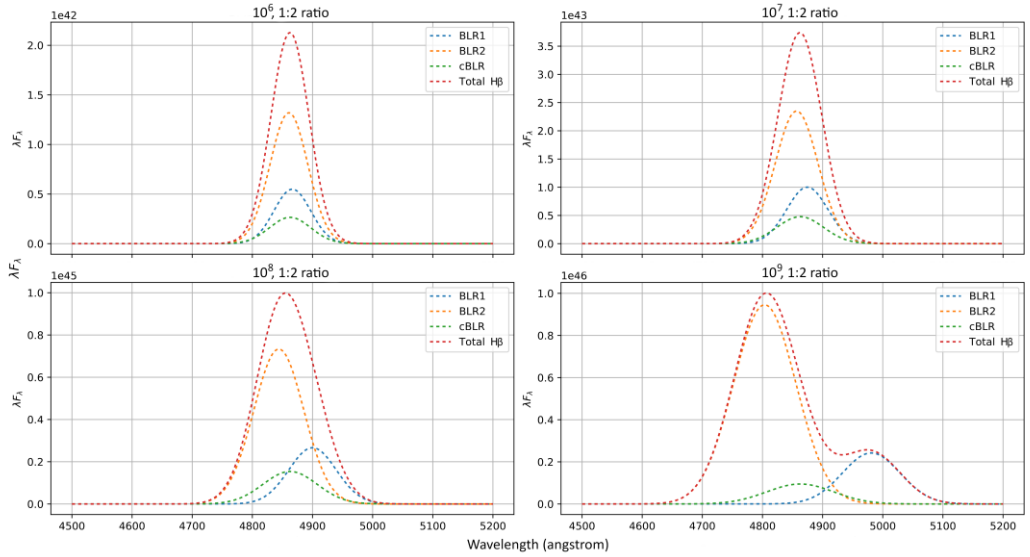

Figure IV.2 The same as Figure IV.1, but with 1:2 mass ratio

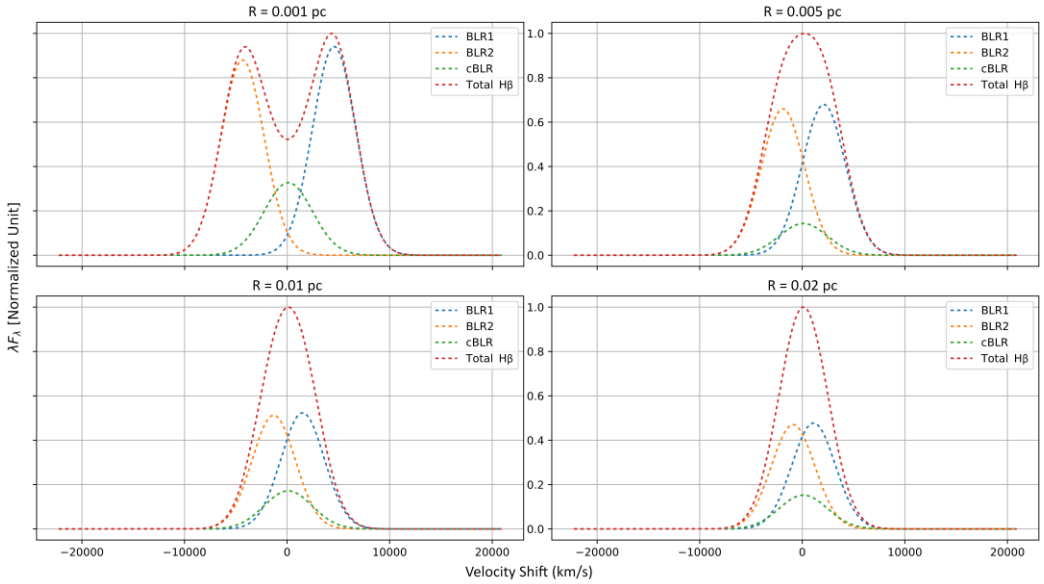

Figure IV.3 Simulated SMBBH spectra to highlight the effect of mean SMBBH separation variation. The spectra are simulated by setting the SMBBH mass to be $10^7 M_\odot$ and 1:1 mass ratio. Spectra are taken at pericentre position for maximum shift. Total Hβ refer to the total emission from the BLR of each component in addition to the circumbinary BLR. Additionally, refer to the top right spectra in Figure IV.1 for the simulated spectra of similar mass configuration at $R = 0.1\ pc$.

4.2.2 Effect of mean separation

Mean separation of SMBBH component affect the broad peak shift, where larger mean SMBBH separation causes less shift in the broad line (see section 2.3.2). According to the radial velocity relation with component mass and mean separation $v_i \propto$

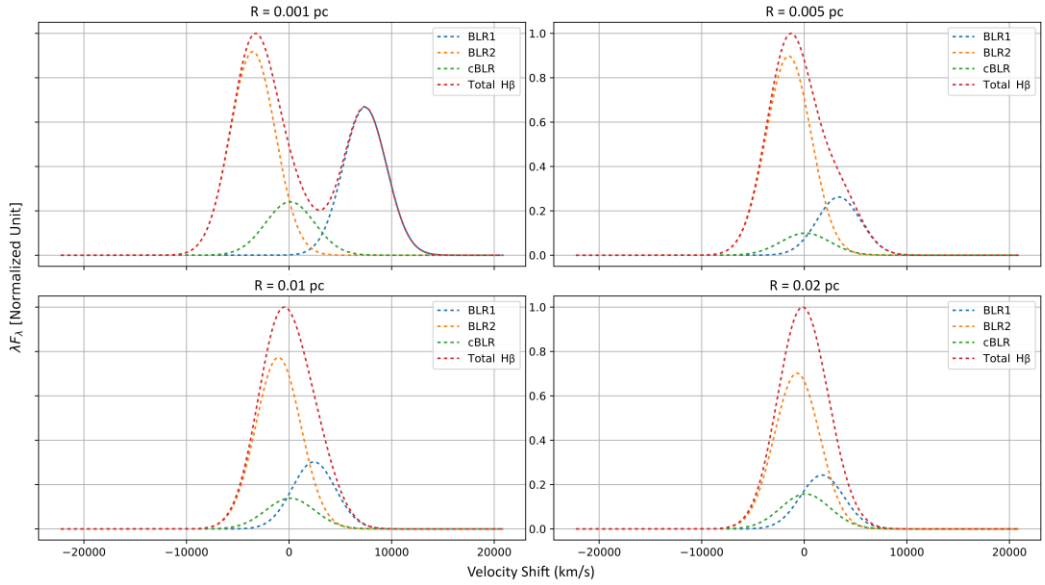

Figure IV.4 The same as Figure IV.3, but with 1:2 mass ratio. Refer to the top right spectra in Figure IV.2 for the simulated spectra of similar mass configuration at $R = 0.1\ pc$.

$R^{-1/2}M_i^{1/2}$established in section 2.3.2, mean separation effect has similar magnitude of effect, only inversed. This means that for a spectrum with a moderately high peak shift, for example, the spectrum may come from a SMBBH system with high mass with high separation, or low mass with low separation. Fortunately, mean separation does not affect broad line width. Therefore, the line width becomes a more reliable mass determination while peak shift shows a combination of effect from mass and mean separation variations.

Figure IV.3 and IV.4 shows how the difference in mean separation affects SMBBH spectra. Due to the moving normalized peak of the component spectra, their width is not visually clear. FWHM measurement shows that all component spectra have FWHM of around 5150 km/s for both components, confirming that changes in mean SMBBH does not change the spectra width.

As previously stated, double peaks might appear for low component mass SMBBH if the mean separation is low enough. SMBBH with $M_i = 10^7 M_\odot$ and 1:1 mass ratio will show a double-peaked spectrum at $R = 0.001\,pc$. Comparing that with the double-peaked spectra of SMBBH with $M_i = 10^9 M_\odot$ and 1:1 mass ratio at $R = 0.1\,pc$ shown in Figure IV.1, double peaks caused by small separation shows spectra with deeper valley between the peaks.

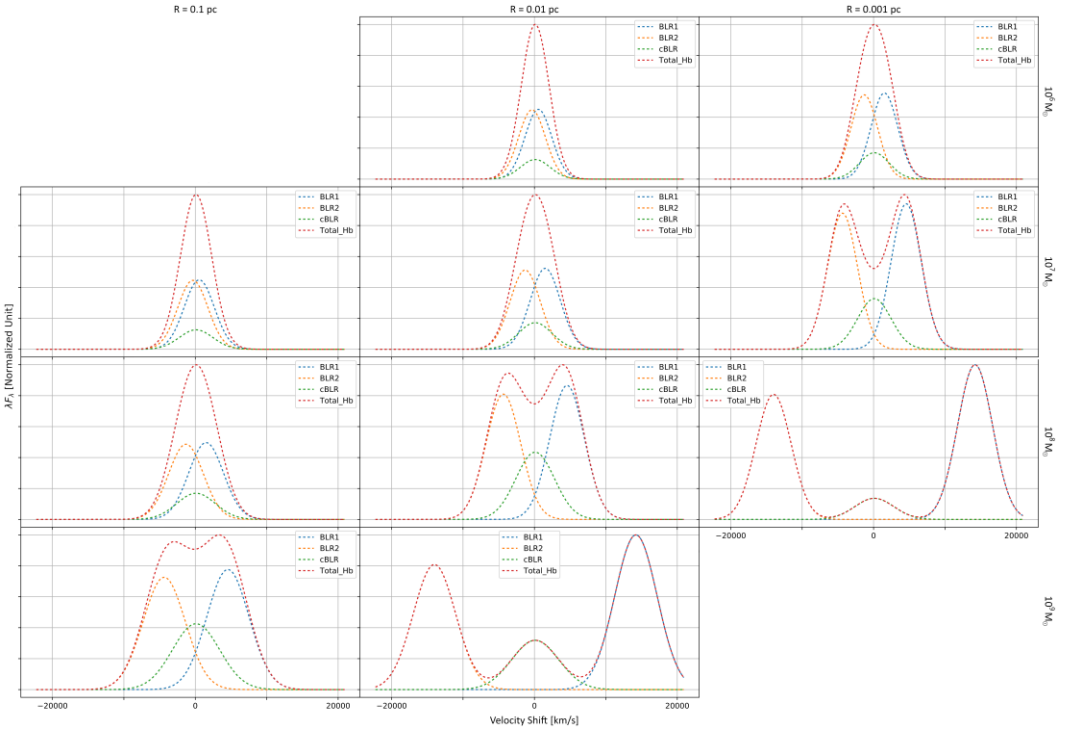

Figure IV.5 Compilation of the effect of mass configuration and mean separation variations. The mass ratio is kept constant at 1:1 ratio. Notice that the diagonals have similar shift for the SMBBH components, while the line width causes the spectra have different total broad Hβ emission.

Due to the relation between radial velocity, mass, and mean separation, certain combination of SMBBH mass and mean separation configuration will give similar peak shift. Specifically, if the M/R is the same, the same peak shift is expected just like the spectra shown in Figure IV.5. Since mean separation only affect peak shift, mass can still be determined by evaluating the line width and, in the case of double peaks, the depth of the valley between the peaks.

4.2.3 Determining SMBBH configuration at the time of detection

Several equations in chapter 2 shows some time-dependent changes in spectra due to parameters that changes over time. This is shown in the spectra peak due to time-dependent changes in effective temperature (see equation II.9 to equation II.13) and

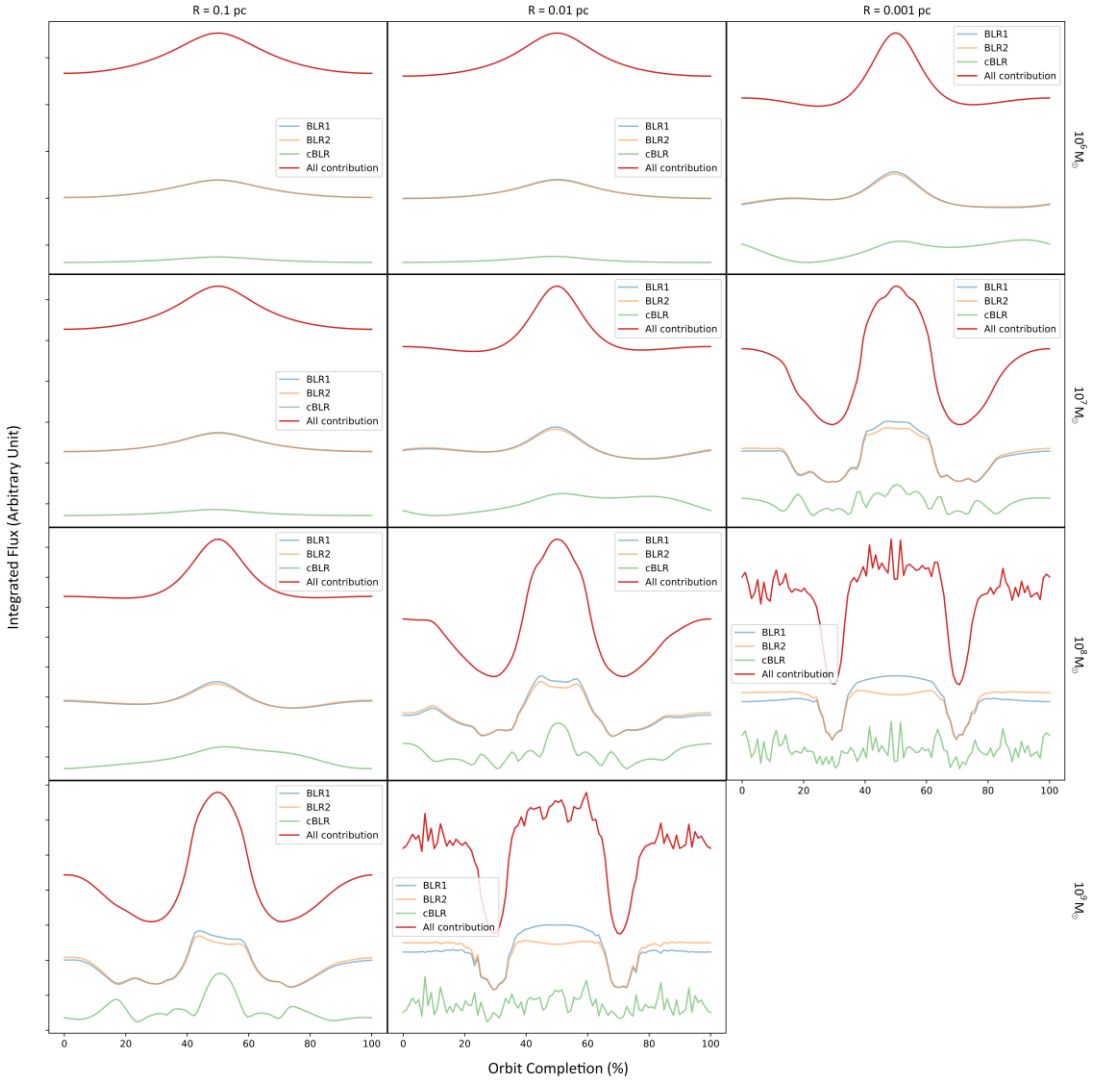

Figure IV.6 Overview of how SMBBH positional configuration, represented by the orbit completion, affect the change of SMBBH spectra line, represented by the integrated flux, of SMBBH with 1:1 mass ratio. The graph is presented in similar way as Figure IV.5.

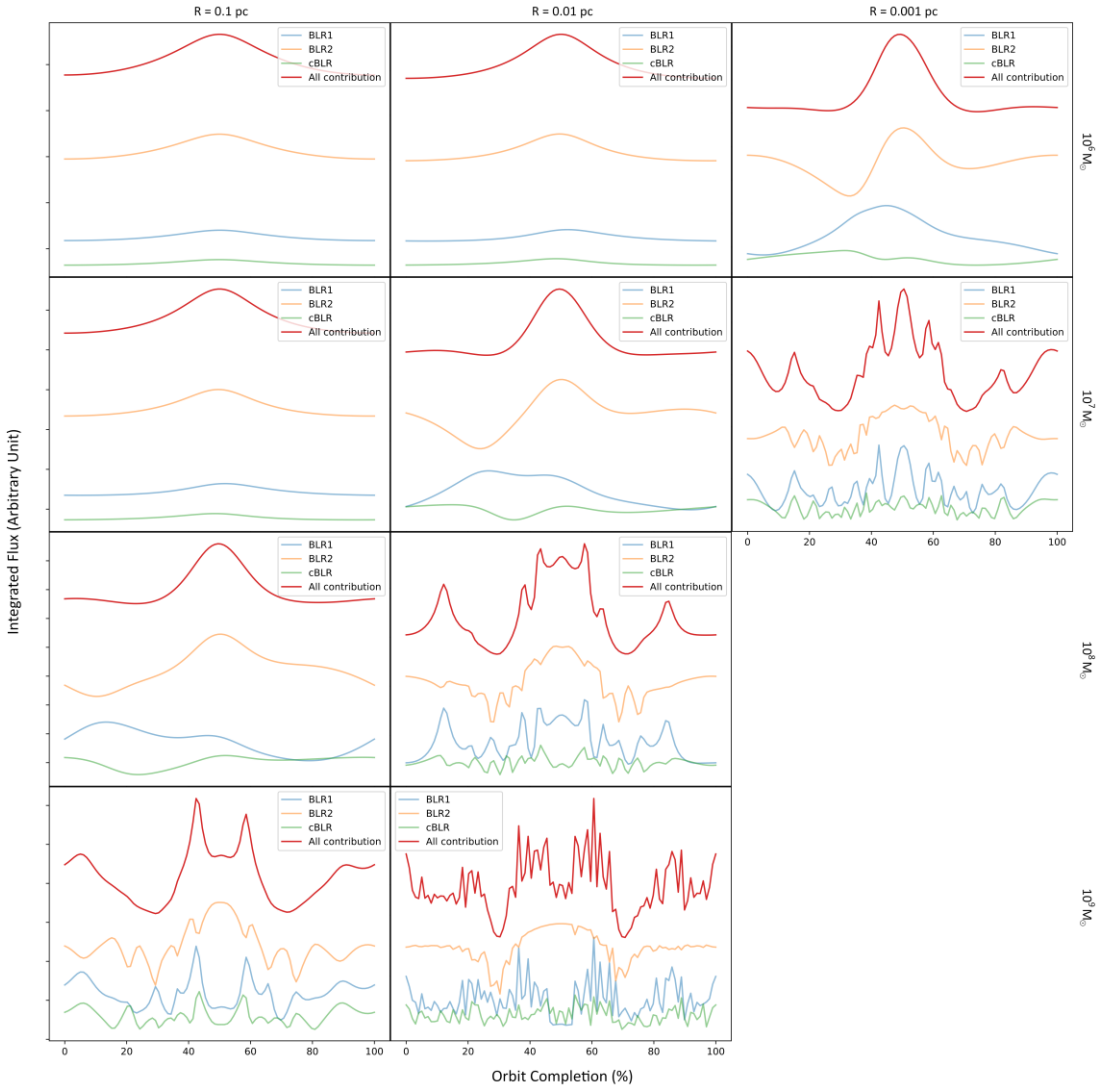

Figure IV.7 The same as Figure IV.6, but for 1:2 mass ratio

spectra peak shift due to time-dependent changes in true anomaly that affected radial velocity (see equation II.5 and II.6).

Figures IV.6 and IV.7 show how position configuration of SMBBH component affect the spectra variety by looking at the how the integrated flux change over time according to PoSKI model. It is interesting to note that for high M/R ratio, the graphs are fluctuating. Apart from the limitation of the numerical simulation, section 2.3.3 shows that the flux peak varies over time, due to the variation of effective temperature over time in addition to the use of the normalized unit. Variation of integrated flux for low M/R component seems to confirm this. Additionally, since double peaks are shown in high M/R ratio, these fluctuations indicate existence of double peaks.

Figure IV.6 and IV.7, although shows that the spectra change over time, do not clearly show how the spectra change. Focusing on positions shown in Figure IV.8, Figure

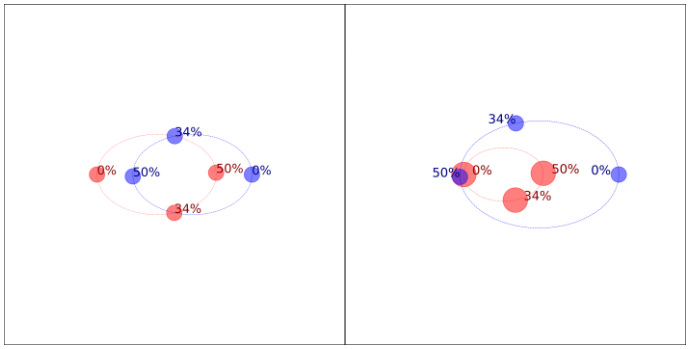

Figure IV.8 Position of SMBBH that are evaluated in Figure IV.9 and IV.10 for 1:1 mass ratio (*left*) and 1:2 mass ratio (*right*)

IV.9 and IV.10 show spectra of SMBBH with $M_i = 10^8\ M_\odot$ mass with mean separation $R = 0.01\ pc$. These figures and Popović (2012) simulations (see Figure III.4) show that observed rest spectra change over time, and therefore the observed SMBBH position can be determined by fitting.

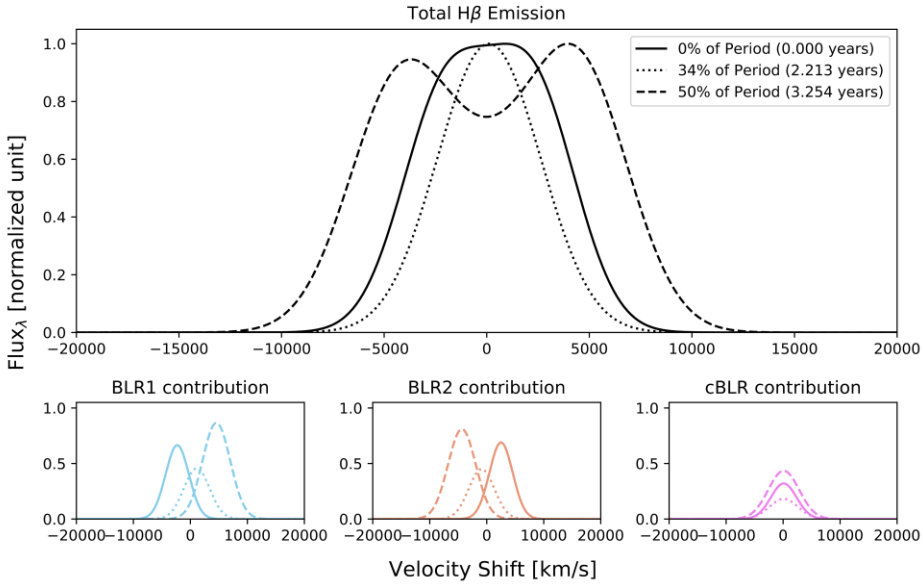

Figure IV.9 Comparison of fluxes at the position highlighted in Figure IV.8 for SMBBH with mass ratio 1:1. The total emission is the observed spectra, while the spectra of each component are highlighted in each of the BLR contribution. The blue and red color in the BLR contribution panels shows which of the SMBH in Figure IV.8 emits the spectra.

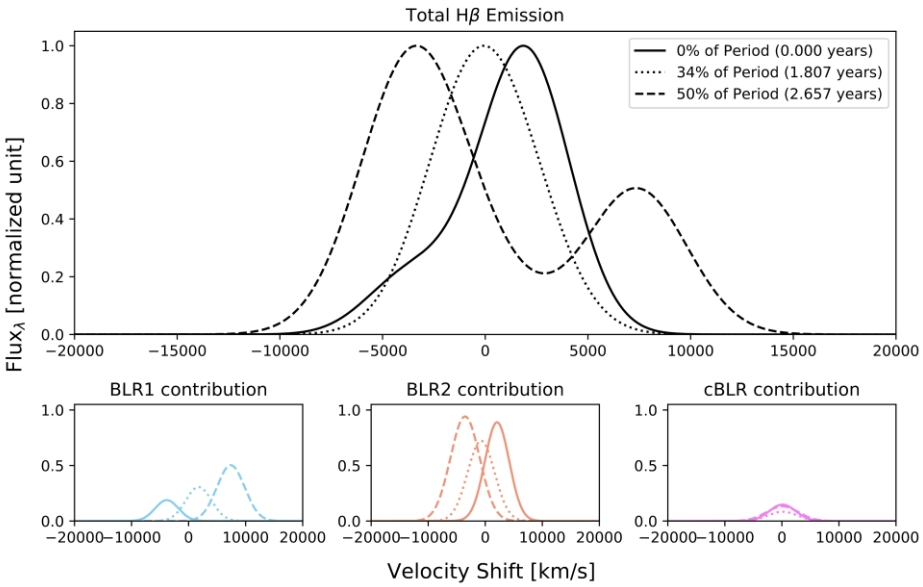

Figure IV.10 The same as Figure IV.9, but with 1:2 mass ratio.

5. Parameter Fitting Result of Observed Spectra with Simulated Spectra

Object spectra that are suspected to be SMBBH candidates that's obtained in chapter 3 is then fitted with simulated spectra discussed in chapter 4. This chapter discusses the fitting procedure and result, while also discussing some of the fitted spectra.

5.1 Extracting broad Hβ component from observed spectra

The Hβ wavelength region is composite from the broad Hβ line which has shape that may indicate emitting region around SMBBHs, but also a number of FeII lines, narrow Hβ and OIII lines at 5007 and 4959 Å. Spectra subtraction is performed to extract the broad Hβ component that is fitted with the PoSKI model. FANTASY package (Ilić et al., 2020; Rakić, 2022; Ilić et al., 2023) allows AGN spectra modelling using specific emitter components. The FANTASY-modelled lines are used to perform the spectra subtraction.

5.1.1 Spectra subtraction with FANTASY

The modelled spectra are assumed to be consisted of the following emission components:

$$I_{Model} = I_{cont} + I_H + I_{He} + I_{Fe} + I_{OIII} \quad (V.1)$$

The hydrogen component can further be expanded into

$$I_H = I_{H\ narrow} + I_{H\ broad}$$

Using the two-component model (Popović et al, 2004), broad Hβ line profile can be modelled with two gaussian-like emission. Therefore,

$$I_{H\ broad} = I_{H\ broad\ 1} + I_{H\ broad\ 2} \quad (V.2)$$

FANTASY assumes a tied model for narrow hydrogen and OIII lines are tied. Therefore,

$$I_{narrow} = H_{H_{narrow}} + I_{OIII}$$

To account for outflows in the narrow emission lines of OIII (Woo et al., 2016):

$$I_{OIII} = I_{OIII\ narrow} + I_{OIII\ outflow}$$

Table V.1 FANTASY parameter settings

Component	Parameter	Fixed Value Set	Tolerance Range
Continuum	Reference Wavelength	5500 angstrom	5490 – 5510 angstrom
Broad 1	Offset[1]	0	-1000 – 1000
	FWHM[2]	2000	1000 – 3000
Broad 2	Offset	0	-1000 – 1000
	FWHM	4000	3000 – 10000
Narrow	Offset	-	0 – 1000
	FWHM	1000	50 – 1500
	Amplitude[3]	-	0.2 – 1000
Helium	Offset	0	-1000 – 1000
	FWHM	2000	1000 – 3000
Iron	Offset	0	-1000 – 1000
	FWHM	2000	1000 – 3000
OIII[5007]	Offset	0	-1000 – 1000
	FWHM	1000	200 – 2000
	Amplitude	-	0.2 – 5000
OIII[4959][4]	Offset	Same as OIII[5007] offset	-
	FWHM	1000	200 - 2000
	Amplitude	1/3.03 of OIII amplitude	

[1]Offset refers to line shift
[2]Line width calculated by the FWHM value
[3]Amplitude at the peak
[4]Secondary OIII are tied with the primary OIII line

For OIII outflow, primary and secondary OIII lines are modelled separately. With $I_{OIII,5007} = 3.03(I_{OIII,4959})$,

$$I_{OIII\ outflow} = I_{OIII,4959} + I_{OIII,5007}$$

Combining all of the above equations, the following components are modelled using FANTASY:

$$I_{Model} = I_{cont} + I_{narrow} + I_{H\ broad\ 1} + I_{H\ broad\ 2} + I_{He} + I_{Fe} + I_{OIII,4959} + I_{OIII,5007} \quad (V.3)$$

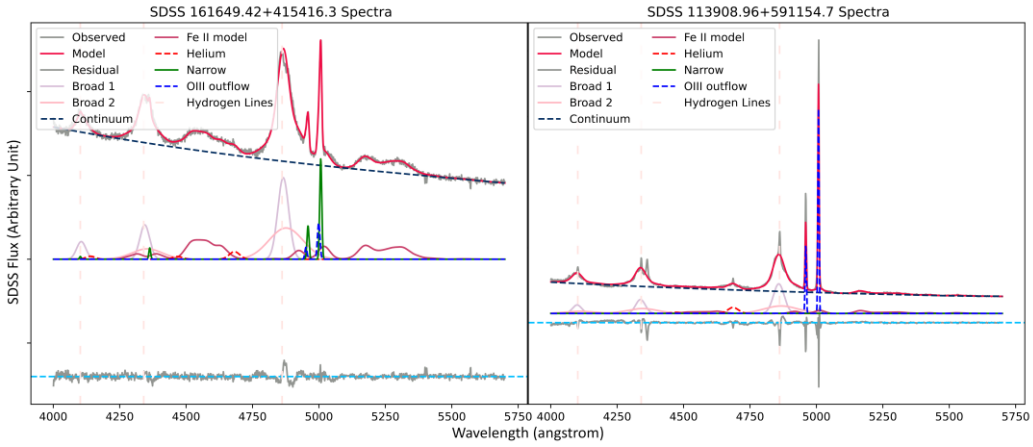

Figure V.1 FANTASY Fitting of 113908.96+591154.7 (*left*) and 161649.42+415416.3 (*right*). Light-blue horizontal line indicates 0 residue. If the residue is close to 0, then the model fit is good.

FANTASY has the following parameters to set in for each emitter components specified in equation V.3. Table V.1 shows the values set for each of the components to generate the FANTASY model.

This FANTASY model generated from $\lambda = 4000 - 5700$ Å. Although the evaluation range of the PoSKI model is only from $\lambda = 4500 - 5200$ Å (see section 4.1), the longer wavelength range is used to accurately model the AGN spectra with FANTASY, due to the inclusion of iron lines that's present around $\lambda = 4500$ Å and $\lambda = 5200$ Å (Ilić et al., 2023). The shorter wavelength range is too close to the iron lines and the iron lines were not properly fitted. Therefore, the longer wavelength range is used to introduce clearance for FANTASY to model the iron lines properly.

FANTASY model spectrum is generated for every SDSS spectra. Figure V.1 show the fitting for two example objects. After a model spectrum $I_{model,i}$ is generated for each SDSS spectra of suspected object $I_{SDSS,i}$, subtraction is done for i-th spectra as follows:

$$I_{subtracted,i} = I_{SDSS,i} - I_{modelsub,i}$$

where $I_{modelsub,i} = I_{Model,i} - (I_{H\ broad\ 1,i} + I_{H\ broad\ 2,i})$, because the subtracted broad is needed. Figure V.2 shows the result of subtraction for objects shown in Figure V.1.

After the spectra is subtracted, the spectra are interpolated and trimmed to 1000 equidistant points between wavelength range of $\lambda = 4500 - 5200$ Å. Assuming FANTASY model has no errors, the error value used is the interpolated error value from the SDSS spectra (see equation A.3).

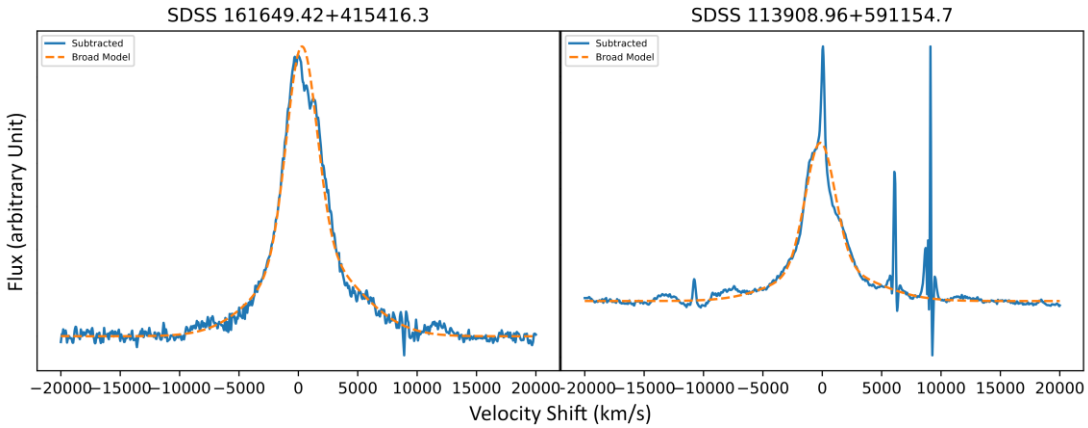

Figure V.2 FANTASY subtraction of spectra shown in figure V.1. The dashed orange lines show broad lines as modelled by FANTASY for comparison.

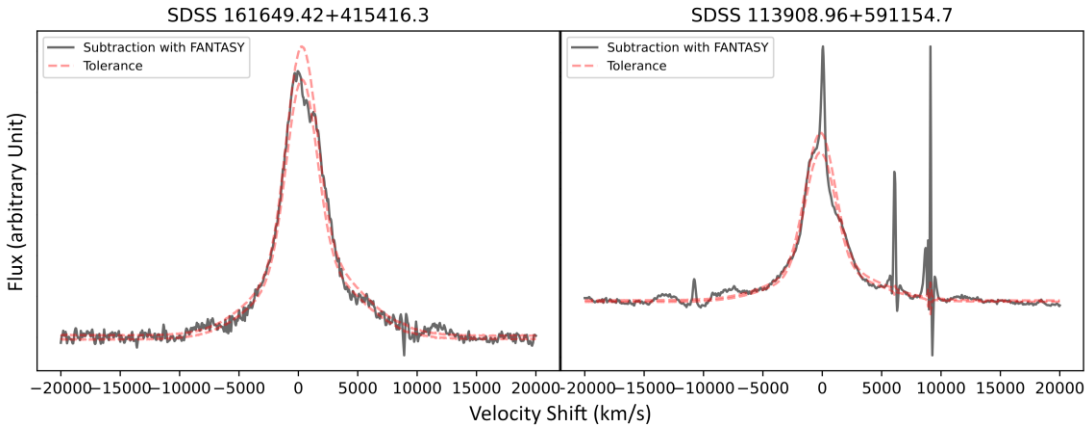

Figure V.3 Process of further subtraction with the aid of FANTASY model of objects shown in figure V.1. The red tolerance lines show the range of acceptable flux. Flux values that fall outside of the red tolerance area is replaced with a random value inside the range.

5.1.2 Additional subtraction of narrow line residuals

Unfortunately, some of the figures are not subtracted properly (see right graph of Figure V.2), especially the narrow lines and OIII lines. While a further refinement of parameters in FANTASY code can be used, a workaround is done. The FANTASY-modelled broad lines are used to simulate the proper spectra. The following equation is used to introduce the flux tolerance at a specific wavelength λ:

$$I^{\pm}_{tol,i}(\lambda) = (1 \pm \tau)\left(I_{broad,i}(\lambda)\right) \pm \sigma_{SDSS,i}/2$$

where τ denotes the tolerance which is set to 5%, and σ_{SDSS} refers to the flux error in the SDSS spectra of object, assuming that $\sigma_{SDSS,i}$ is equally spread around the FANTASY modelled components shown in equation V.3. If the observed flux $I_{SDSS,i}(\lambda)$ falls outside the $I^{\pm}_{tol,i}(\lambda)$, it will be replaced with random value between the maximum $I^{+}_{tol,i}(\lambda)$ and minimum $I^{-}_{tol,i}(\lambda)$ to simulate noise. Figure V.3 this process applied to objects shown in Figure V.1.

5.2 Broad Hβ fitting with PoSKI model

Extracted Hβ broad lines dubbed $I_{SDSS,broad}(\lambda)$ are then normalized to the maximum flux value of each spectrum. These $I_{norm}(\lambda)$ spectra are then fitted with 360 available simulated spectra $I_{sim}(\lambda)$ with various configurations discussed in chapter 4. The χ^2 value for each normalized spectrum $I_{norm,n}(\lambda)$ that is fitted with each simulated spectrum $I_{sim,m}(\lambda)$ is obtained with the following equation:

$$\chi^2_{n,m} = \sum_{i}^{1000}\left(I_{norm,n}(\lambda_i) - I_{sim,m}(\lambda_i)\right)^2$$

Table V.2 Confidence level of fitting

χ^2	Confidence Level
< 1	Very High
1-2	High
2-3	Low
> 3	Very Low

Parameters of $I_{sim,m}(\lambda_i)$ that gives minimum $\chi^2_{n,m}$ value for $I_{norm,n}(\lambda_i)$ is determined to be the SMBBH parameters that produces $I_{norm,n}(\lambda_i)$, and therefore is defined as the SMBBH parameters of the object. This search is implemented using an original Python 3.0 code.

Table V.2 shows how good the fit is based on the χ^2 value. This is an arbitrary classification but can indicate a level of confidence on the parameters of the SMBBH system fitted. A high level of confidence assumes that the spectrum comes from a SMBBH system with the fitted parameters, while a low level of confidence suggests that the spectrum might not come from a SMBBH system, or, in the case that it does, the fitted parameters are erroneous. Appendix C shows the classification of the SMBBH spectra with the parameters and confidence level for all of the SMBBH candidates obtained from the SDSS DR16 QSO catalogue.

5.2.1 High confidence fit

Out of 294 objects in classified as suspected SMBBH candidates, 57 objects are fitted with high and very high level of confidence. Accounting for the duplication in double-peaked objects (see section 5.2.2.3 for further discussion) there are 270 distinct objects, with 54 well-fitted objects. Table V.3 shows the number of objects with good fits for each spectra selection criteria discussed in section 3.2.3, with the inclusion of the double-peaked duplication, while Figure V.4 shows example of objects with “very high” and “high” confidence level of fitting for each object spectra selection criteria.

5.2.1.1 High confidence parameters

With a high confidence level of fitting, the SMBBH fitted with the model should have a parameter very close with the fitting parameters, especially the component mass, mass

Table V.3 Numbers objects with high confidence fit

Selection Criteria	Number of Objects	High-confidence Fits
Eracleous Objects	159	27
Double Peaks	29	4
Asymmetric	75	15
Broad	31	11

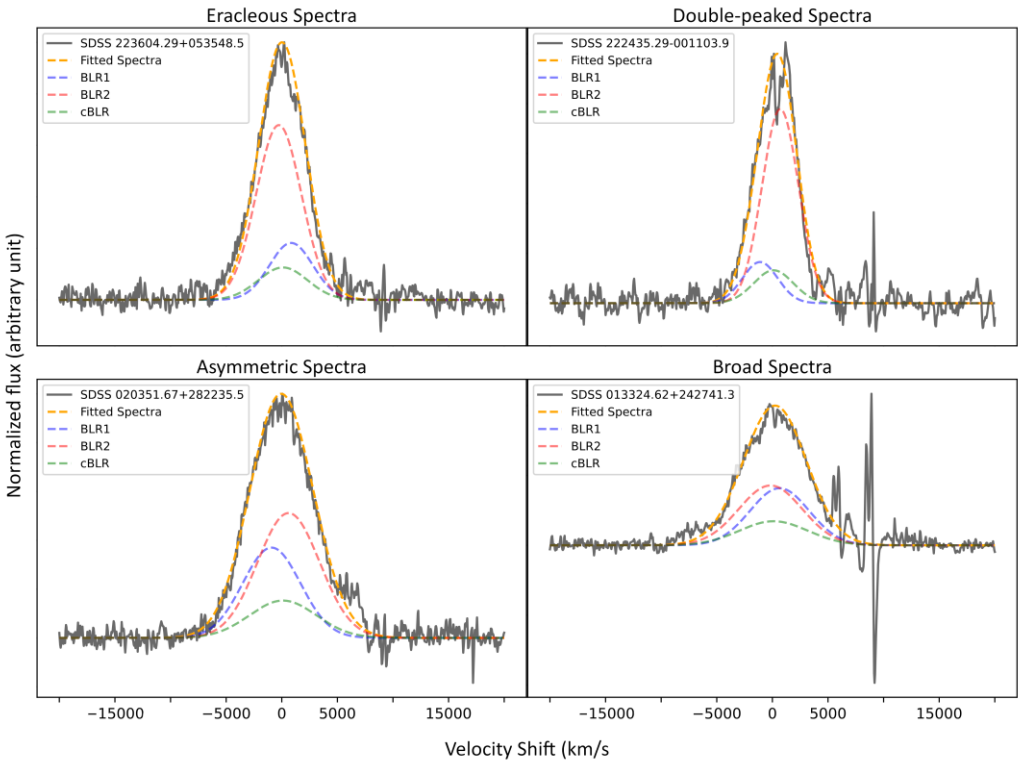

Figure V.4 Example of objects with good fits. The object spectra shown is the FANTASY-subtracted spectra and therefore, some residue of OIII lines can be seen (especially prominent in *Broad Spectra* fitting).

ratio, and component separation. It is also interesting to note whether highly peculiar broad Hβ line profile, indicated by the high M/R ratio, is more common than less peculiar spectra, indicated by the low M/R ratio.

Table V.4 makes notes of how many of objects have specified parameters. The detection spread of component mass seems to be somewhat even for Eracleous object compared to the high number of detections of SMBBH with low ($10^6\ M_\odot$) component mass. However, spectra with somewhat high peculiarity (with $M/R = 10^9$ and $M/R = 10^{10}$) are more commonly detected than lower peculiarity. This suggests that the fitting might be more sensitive towards peak shift than masses, with the very highly peculiar spectra seems to be less common.

Additionally, Kazantzidis (2005) noted that unequal mass mergers are more effective at building gas reservoir for SMBH accretion due to the significant frequency of unequal mass merger compared to equal mass merger in the hierarchical structure formation model. Table V.4 shows that the fitting detects more SMBBH systems with uneven mass (1:2 mass ratio) compared to the even mass SMBBH (1:1 mass ratio). This amount confirms the validity of Kazantzidis (2005) statement.

Table V.4 Number of high-confidence object with parameters.

Parameters	Eracleous Objects	Double Peaks Objects	Asymmetric Objects	Broad Objects	Total
Component Mass ($M_\odot$)					
10^6	7	1	8	5	*21*
10^7	8		3	2	*13*
10^8	6		2	1	*9*
10^9	6		2	3	*11*
Component Mass Ratio					
1:1	4		5	3	*12*
1:2	23	1	10	8	*42*
Component Separation (pc)					
0.001	9	1	3	2	*15*
0.005	5		3	1	*9*
0.01	4		2	1	*7*
0.02	2		0	1	*3*
0.1	7		7	6	*20*
M/R[1]					
1×10^7	3		5	3	*11*
1×10^8				1	*1*
2×10^8			2		*2*
5×10^8	1				*1*
1×10^9	7	1	2	3	*13*
2×10^9	1			1	*2*
1×10^{10}	7		5	1	*13*
2×10^{10}	4		1		*5*
5×10^{10}	1			1	*2*
1×10^{11}	3			1	*4*

[1]While other M/R value exists, this table only list the values that have at least 1 object.

The fitting seems to be more sensitive towards the extremes in peak shift, indicated by the most and 2nd most common component separation being the 0.1 pc and 0.001 pc separation. In addition, the 15 objects with 0.001 pc separation, and some objects with 0.005 pc separation to some extent, might be interesting for future studies since imminent mergers might happen. Table V.5 lists the 15 high-confidence objects with separation of 0.001 pc.

5.2.1.2 High confidence fit with visually bad fit

Although it was stated previously that high confidence fit guarantees the SMBBH parameters, further analysis needs to be done to confirm the parameter determination. An indication of this is the presence of equal-mass SMBBH detected for object with spectra asymmetry. As discussed in section 4.2.1, asymmetry occur only for unequal mass

Table V.5 High-confident objects with component separation of 0.001 pc or 0.005 pc

Component Separation	Eracleous Objects[1]	Asymmetric Objects[1]
0.001 pc	• 123516.14+462309.3 • 231821.08+322339.5 • 095048.38+392650.4 • 020840.66-062716.7 • 110436.33+212417.8 • 081501.85+525255.5 • 110539.81+342534.6 • 150527.60+294718.3 • 020412.45+224226.1	• 074455.95+364743.8 • 161425.17+375210.7 • 103440.91+443105.0
0.005 pc	• 223604.29+053548.5 • 093728.57+324548.3 • 010312.99+022109.9 • 231101.69+182744.6 • 233908.79-000637.8	• 015910.06+010514.5 • 130947.00+081948.2 • 092809.43+383000.5
Component Separation	**Double Peaks Objects[1]**	**Broad Objects[1]**
0.001 pc	• 125157.90+061341.6	• 222435.29-001103.9 • 012648.09+032706.7
0.005 pc		• 135529.06+352332.1

[1]Object name uses the SDSS coordinate designation

SMBBH. Limitation of the simulation can produce spectra asymmetry on equal mass component (see figure IV.5, especially on high M/R parameters).

Some high-confidence spectra shown in appendix C shows bad visual fit (see figure C.1 to C.4). Simulation limitation alone does not explain the bad visual fit. Instead, these inaccuracies seem to happen due to bad method of spectra subtraction. Due to the additional subtraction process by fitting the spectra with broad models by FANTASY, some of the peculiarities may not be preserved, especially for spectra with double peaks (see section 5.2.2.3 for further discussion).

5.2.2 Low confidence fit

Figure V.5 shows example of objects with “very low” and “low” confidence level of fitting. Some of these low confidence fit may be attributed to a highly noisy spectra as seen in or a high level of error in observation, causing the spectra subtraction to be inaccurate. An example of both can be seen in Figure V.6. However, other low-confidence fittings are analyzed in a case-by-case basis. In the subsequent subsections, three general cases of bad fit are explored further.

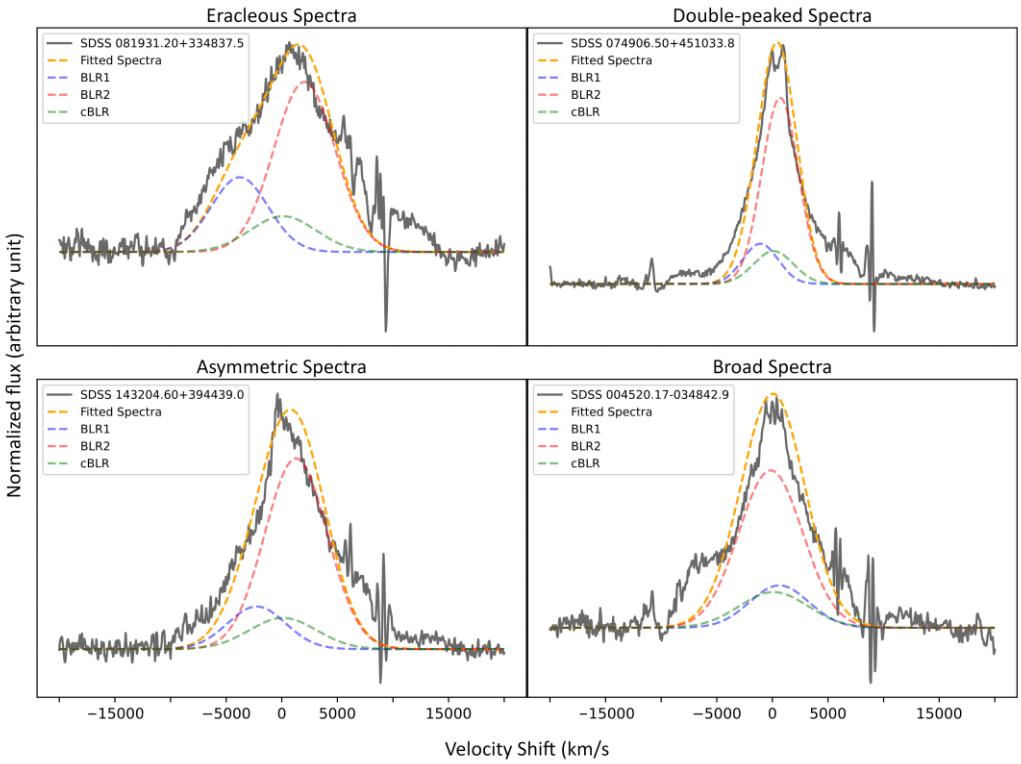

Figure V.5 The same as figure V.4 but with low-confidence fitted spectra.

5.2.2.1 Spectra width

Some of the bad fit was caused by the inaccurate fitting of spectra width, with Some spectra are too narrow to be fitted while others are too broad. An example of both can be seen in Figure V.7. Due to limitation in spectra simulation, SMBBH with component mass $10^6\ M_\odot < M_i < 10^9\ M_\odot$ cannot be simulated properly. This suggest that, if the spectra come from SMBBH system, there exists a SMBBH with the component mass less than $10^6\ M_\odot$ or more than $10^9\ M_\odot$.

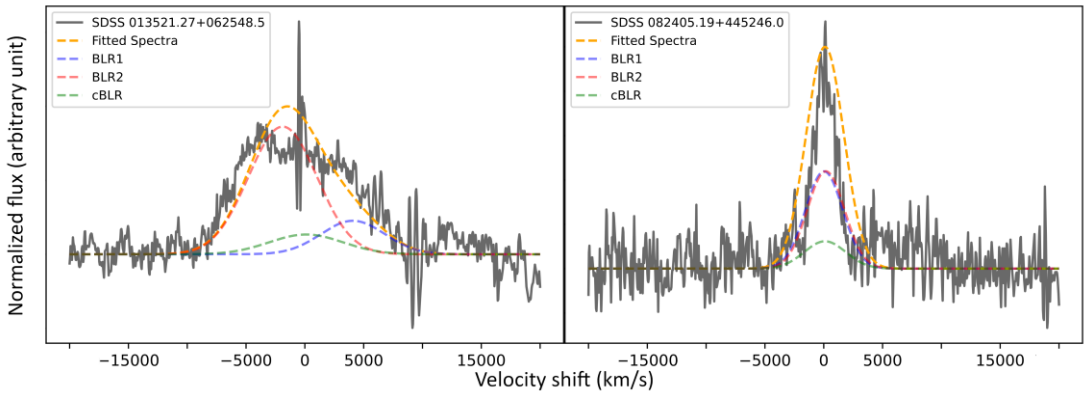

Figure V.6 Example of object with bad fits due to high large observation error (*left*) and noisy spectra (*right*).

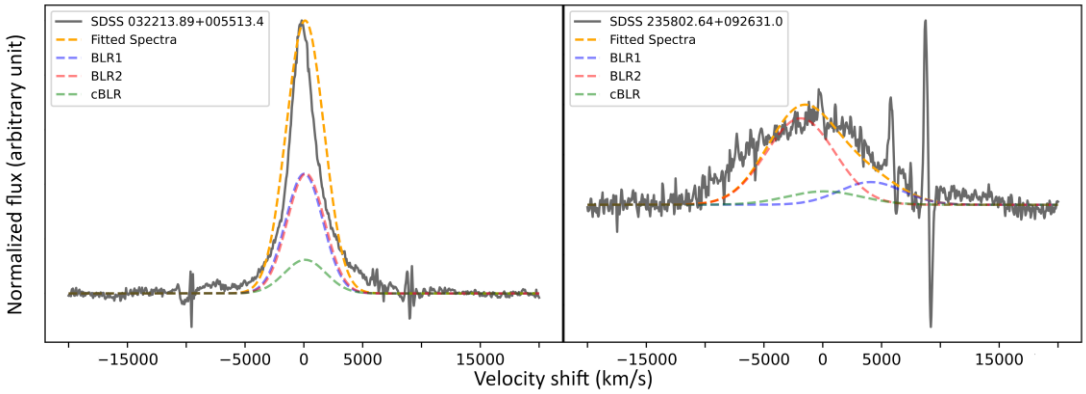

Figure V.7 Example of badly fitted spectra due to the spectra being too narrow (*left*) or and too broad *(right*). Simulated spectra with minimum component broadening (using $M_i = 10^6\ M_\odot$) is used for the left spectra while simulated spectra with the maximum component broadening (using $M_i = 10^9\ M_\odot$) is used for the right spectra.

5.2.2.2 Spectra asymmetry

Another cause of bad fit is the inaccurate fitting of asymmetry. Figure V.8 shows an example of these poor fit where asymmetry is not correctly reproduced with the fitting.

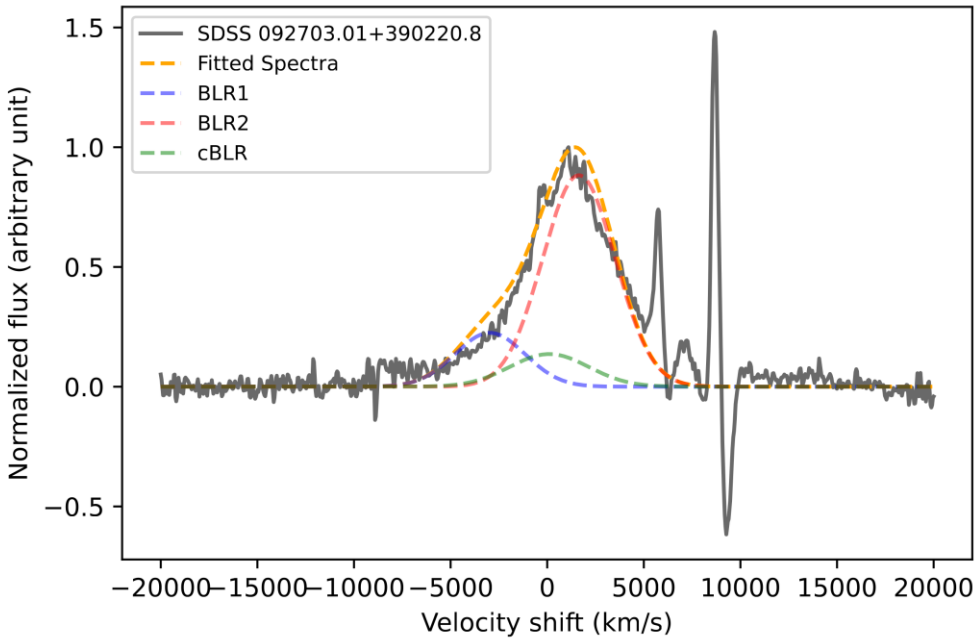

Figure V.8 Example of bad fit due to wrong asymmetry. Notice that the for the subtracted spectra, the left side appears to be broader than the right side.

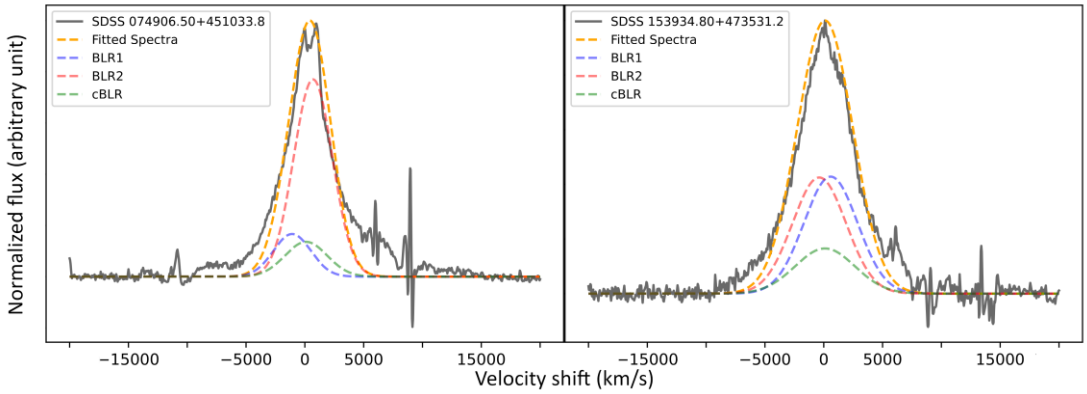

Figure V.9 Examples of object which broad H-beta base is too broad. Object on the left has a low-confidence fit while object on the right has a high-confidence fit.

The simulation only shows a specific SMBBH configuration for 1:2 mass ratio, where the smaller SMBBH component's starting position is on the right of the bigger component. Opposite radial velocity causes shift in the opposite direction (see equation II.2). Therefore, since this condition is not simulated, the fitting with simulated spectra is bad.

In addition, most of the spectra seemed to have a wider base than simulated spectra, causing a bad fit. Popović et al. (2004) noted that the AGN BLR is quite complex. While FANTASY modelling addresses this with two-component model, the simulated spectra still seemingly assume a single gaussian model for one SMBBH component (see equation II.2). Therefore, a simulated spectra with two-gaussian model for each SMBBH component might produce a better fit. However, this also happens with high-confidence fits (see Figure V.9). This means that some of the objects with high-confidence fits might

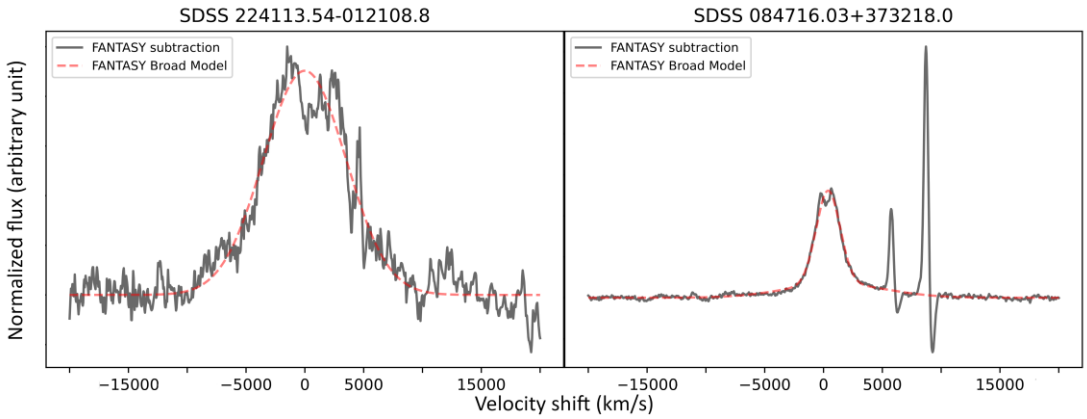

Figure V.10 Illustration of the problem with the double-peaked objects. For the right objects, double peaks are still clear even with relatively noisy image. Notice that the FANTASY broad model, which is used as the base for the further subtraction, does not recreate the double peaks from the FANTASY subtraction.

produce inaccurate SMBBH parameters, reinforcing the need for further analysis, even for good fits.

5.2.2.3 Case of double-peaked spectra

Amongst all of the SMBBH candidates' classification, objects with double-peaked spectra have the worst fit, with 24 out of 29 double-peaked objects have very low to low confidence level. Further investigation revealed that due to the further subtraction with FANTASY model, double peaks are not recreated (see Figure V.10). This also happens in high-confidence fits, making the parameters determination for double-peaked spectra not reliable. Therefore, a better spectra subtraction needs to be performed in order to properly analyze the double peaks. In addition, a better spectra subtraction method is also needed for the high confidence object for a more reliable and accurate parameter determination of SMBBH systems.

Additionally, some objects with double peaked seems to be duplicate of other object classification (see appendix C). This duplicate not only happens in low-confidence fitting, but also in high confidence fitting. This indicates that double peaks in spectra are often accompanied with other spectra peculiarities. Further investigation shows that these objects have the same mass and separation parameters with their duplicates, with few of them have different position in year. This difference in year can be attributed to the randomness introduced in the additional subtraction phase (see section 5.1.2) since the duplicates are fitted twice, as different objects.

5.2.3 Comparison with previous catalogue of SMBBH candidates

From Eracleous et al. (2012), 88 objects were classified as SMBBH candidates. Out of these objects, 30 objects have $SNR > 30$, and 16 objects are classified as SMBBH candidates in this thesis. The 16 objects include objects with minor discrepancies in the SDSS designation where the designation from SDSS DR7 QSO catalogue and the SDSS DR16 QSO catalogue differ by 0.01 second for the RA or 0.1 second for the declination. Since the difference is minuscule, it is assumed that objects with these discrepancies are the same object. Some of the unavailability of the objects might be due to misclassifications, erroneous data filtering, or data corruption.

Table V.6 shows the parameters and confidence level of these objects, sorted by the object parameters. Although in general, the confidence levels of these objects are low, it is interesting to note what kind of objects are prioritized by Eracleous criteria. All of

Table V.6 Parameters of objects from Eracleous et al. (2012)

SDSS designation	M_i ($\log M_\odot$)	Mass Ratio	R (pc)	Position (Year)	χ^2	Confidence
095539.82+453216.9	7	1:2	0.001	0.388	4.841	Very Low
171448.50+332738.3[1,3]	7	1:2	0.001	0.388	5.063	Very Low
130534.49+181932.8	7	1:2	0.001	0.122	5.141	Very Low
160243.91+174503.9	7	1:2	0.001	0.191	5.568	Very Low
161911.24+501109.2	7	1:2	0.01	9.243	2.137	Low
140251.19+263117.5[1]	8	1:2	0.005	1.447	3.019	Very Low
140700.40+282714.6[1]	9	1:2	0.01	1.244	1.394	High
153636.22+044127.0[1,2]	9	1:2	0.01	1.109	3.687	Very Low
002444.11+003221.2	9	1:2	0.02	1.616	2.100	Low
093653.84+533126.8	9	1:2	0.02	1.331	2.218	Low
113330.30+105223.3	9	1:2	0.02	1.616	2.738	Low
075403.60+481428.0	9	1:2	0.02	3.090	3.064	Very Low
120924.07+103612.0	9	1:2	0.02	1.331	5.649	Very Low
015530.02-085704.0	9	1:2	0.1	12.223	2.802	Low
151443.06+365050.4	9	1:2	0.1	18.601	3.433	Very Low
133432.34+171146.9[2]	9	1:2	0.1	19.132	3.509	Very Low

[1]These objects have the same designations as the one used by Eracleous et al. (2012). The rest of the object designations are off by 0.01 seconds RA or 0.1 seconds declination

[2]Objects are also classified as having double peaks

[3]Object is misidentified as *broad object*

Eracleous objects shown in table V.6 are fitted with 1:2 mass ratio, with 10 out of 16 objects have component mass of $10^9\ M_\odot$. Additionally, 7 out of 16 objects have $M/R = 10^{10}$ with another 6 objects have the same order of magnitude. With this, it is shown that Eracleous criteria for SMBBH candidates works best for objects with highly peculiar broad Hβ line profile, which shows either high mass SMBBH, very close SMBBH, or both. In addition, Eracleous criteria works better for certain SMBBH positional configuration, especially the configuration close to the pericenter due to the significant peak shift.

6. Conclusions and Suggestions for Future Studies

6.1 Conclusions

In this thesis, an updated search of suspected SMBBH candidates from SDSS DR16 QSO catalogue was done. Additionally, PoSKI model of SMBBH was studied in order to estimate the parameters of SMBBH from its broad Hβ line profile, particularly the mass, mass ratio, and mean separation of its SMBH component, in addition to the positional configuration of the component. The steps done to determine the parameters of SMBBH candidates from SDSS DR16 QSO catalogue are as follows:

1. Objects with $z < 0.8$ from the SDSS DR16 QSO catalogue were filtered using PCA, selecting objects with $SNR > 30$ and poorly reconstructed spectra, particularly around the Hβ wavelength.
2. The selected spectra were preprocessed with the FANTASY code to shift the spectra to rest wavelength, deredden, and extracting the broad Hβ lines by subtracting narrow Hβ lines and various satellites lines. Additional subtraction using a FANTASY-modelled broad Hβ line was also performed.
3. Simulated spectra were generated using the PoSKI model, varying mass, mass ratio, component separation, and SMBBH configuration.
4. The preprocessed spectra were fitted to the simulated ones, with the best-fitting parameters identified as the SMBBH parameters for each of the sample spectra.

Out of 76466 SDSS objects, 270 objects are chosen as samples. These objects are categorized with the following criteria:

- 159 objects exhibit spectra similar to spectra described by Eracleous et al. (2012).
- 29 objects show evidence of double peaks in the broad Hβ line profile. These objects include 24 duplicate objects showing Eracleous, asymmetric, or very broad Hβ line profile.
- 75 objects show asymmetry in the broad Hβ line profile.
- 31 objects show a very broad Hβ line profile.

After determining the parameters of the sample objects, the main findings are as follows:

- 54 objects are fitted with high level of confidence, meaning that there is a good chance that sub-parsec SMBBH systems are present in these objects with parameters very close to the ones determined in this thesis. However, further study and scrutiny of these objects are encouraged since other effect can contribute to the unusual Hβ line profile.
- 24 high-confidence objects are determined to have component separation of 0.001 or 0.005, suggesting that these objects might undergo mergers quite soon.
- PoSKI is shown to be capable of simulating broad Hβ line profile in various stage in its revolution period, making it capable to predict the broad Hβ line profile in the future, and can be used for additional observation to confirm the existence of SMBBH systems.

6.2 Suggestions

This thesis is still open for future improvement and discussion. The following suggestions can be implemented in future works:

- A more reliable method of PCA, especially the need of proper normalization and threshold for fitting can be developed to reduce the number of objects that has to be visually filtered to obtain the SMBBH candidates from SDSS spectra.
- Proper spectra subtraction method is needed to have a properly reduced spectra that still preserve the broad Hβ peculiarity, while simultaneously fully subtract the narrow Hβ line and OIII lines.
- Other effects that might give rise to unusual Hβ profile should be checked. This might explain the inaccurate subtractions of narrow Hβ and OIII lines.
- More variations with input parameters of simulated spectra should be explored, as this might improve the confidence level of fitting.
- Objects labelled with high and very high level of confidence can be candidates for future observations to further confirm the existence of SMBBH systems in these objects. This can be done by analyzing the current and the future (or if available, the past) spectroscopic observations of these objects and comparing them with the simulated spectra using PoSKI model.
- Some objects noted in table V.5 can be observed for extended period to further confirm the existence of SMBBH systems in them. If SMBBH systems are confirmed, these objects should be further observed as they might undergo mergers soon.

Bibliography

Afanasiev, V. L., Popović, L. Č., & Shapovalova, A. I. (2018). Spectropolarimetry of Seyfert 1 galaxies with equatorial scattering: black hole masses and broad-line region characteristics. *Monthly Notices of the Royal Astronomical Society*, *482*(4), 4985–4999. https://doi.org/10.1093/mnras/sty2995

Almeida, A., Anderson, S. F., Argudo-Fernández, M., Badenes, C., Barger, K., Barrera-Ballesteros, J. K., Bender, C. F., Benitez, E., Besser, F., Bird, J. C., Bizyaev, D., Blanton, M. R., Bochanski, J., Bovy, J., Brandt, W. N., Brownstein, J. R., Buchner, J., Bulbul, E., Burchett, J. N., . . . Zasowski, G. (2023). The Eighteenth Data Release of the Sloan Digital Sky Surveys: Targeting and First Spectra from SDSS-V. *The Astrophysical Journal Supplement Series*, *267*(2), 44. https://doi.org/10.3847/1538-4365/acda98

Begelman, M. C., Blandford, R. D., & Rees, M. J. (1980). Massive black hole binaries in active galactic nuclei. *Nature*, *287*(5780), 307–309. https://doi.org/10.1038/287307a0

Bon, E., Popović, L. Č., Gavrilovi, N., La Mura, G., & Mediavilla, E. (2009). Contribution of a disc component to single-peaked broad lines of active galactic nuclei. *Monthly Notices of the Royal Astronomical Society*, *400*(2), 924–936. https://doi.org/10.1111/j.1365-2966.2009.15511.x

Boroson, T. A., & Lauer, T. R. (2010). EXPLORING THE SPECTRAL SPACE OF LOW REDSHIFT QSOs. *The Astronomical Journal*, *140*(2), 390–402. https://doi.org/10.1088/0004-6256/140/2/390

Burke-Spolaor, S. (2010). A radio Census of binary supermassive black holes. *Monthly Notices of the Royal Astronomical Society*, *410*(4), 2113–2122. https://doi.org/10.1111/j.1365-2966.2010.17586.x

Collin, S., Kawaguchi, T., Peterson, B. M., & Vestergaard, M. (2006). Systematic effects in measurement of black hole masses by emission-line reverberation of active galactic nuclei: Eddington ratio and inclination. *Astronomy and Astrophysics*, *456*(1), 75–90. https://doi.org/10.1051/0004-6361:20064878

Dobbie, P. B., Kuncic, Z., Bicknell, G. V., & Salmeron, R. (2009). Enhanced MHD transport in astrophysical accretion flows: turbulence, winds and jets. *Plasma and Fusion Research*, *4*, 017. https://doi.org/10.1585/pfr.4.017

Eracleous, M., Boroson, T. A., Halpern, J. P., & Liu, J. (2012). A LARGE SYSTEMATIC SEARCH FOR CLOSE SUPERMASSIVE BINARY AND RAPIDLY RECOILING BLACK HOLES. *The Astrophysical Journal Supplement Series*, *201*(2), 23. https://doi.org/10.1088/0067-0049/201/2/23

Fitzpatrick, E. L. (1999). Correcting for the effects of interstellar extinction. *Publications of the Astronomical Society of the Pacific*, *111*(755), 63–75. https://doi.org/10.1086/316293

Francis, P. J., Hewett, P. C., Foltz, C. B., & Chaffee, F. H. (1992). An objective classification scheme for QSO spectra. *The Astrophysical Journal*, *398*, 476. https://doi.org/10.1086/171870

Fu, H., Zhang, Z. -Y, Assef, R. J., Stockton, A., Myers, A. D., Yan, L., Djorgovski, S. G., Wrobel, J. M., & Riechers, D. A. (2011). A KILOPARSEC-SCALE BINARY ACTIVE GALACTIC NUCLEUS CONFIRMED BY THE EXPANDED VERY LARGE ARRAY. *The Astrophysical Journal Letters*, *740*(2), L44. https://doi.org/10.1088/2041-8205/740/2/l44

Gaskell, C. M. (2008). Accretion Disks and the Nature and Origin of AGN Continuum Variability. *The Nuclear Region, Host Galaxy and Environment of Active Galaxies (Eds. Erika Benítez, Irene Cruz-González, & Yair Krongold) Revista Mexicana de Astronomía y Astrofísica (Serie de Conferencias)*, *32,* 1-11, https://doi.org/10.48550/arXiv.0711.2113

Gaskell, C. M. (2009). What broad emission lines tell us about how active galactic nuclei work. *New Astronomy Reviews*, *53*(7–10), 140–148. https://doi.org/10.1016/j.newar.2009.09.006

Gewers, F. L., Ferreira, G. R., De Arruda, H. F., Silva, F. N., Comin, C. H., Amancio, D. R., & Da F Costa, L. (2021). Principal component analysis. *ACM Computing Surveys*, *54*(4), 1–34. https://doi.org/10.1145/3447755

Giuliani, L., Ghisellini, G., & Sbarrato, T. (2021). A new panchromatic classification of unclassified Burst Alert Telescope active galactic nuclei. *Astronomy and Astrophysics*, *647*, A195. https://doi.org/10.1051/0004-6361/202037912

Hilditch, R. W. (2001). *An introduction to close binary stars*. Cambridge University Press.

Ilić, D., Oknyansky, V., Popović, L. Č., Tsygankov, S. S., Belinski, A. A., Tatarnikov, A. M., Dodin, A. V., Shatsky, N. I., Ikonnikova, N. P., Rakić, N., Kovačević, A., Marčeta-Mandić, S., Burlak, M. A., Mishin, E. O., Metlova, N. V., Potanin, S. A., & Zheltoukhov, S. G. (2020). A flare in the optical spotted in the changing-look Seyfert NGC 3516. *Astronomy and Astrophysics*, *638*, A13. https://doi.org/10.1051/0004-6361/202037532

Ilić, D., Rakić, N., & Popović, L. Č. (2023). Fantastic Fits with fantasy of Active Galactic Nuclei Spectra: Exploring the Fe ii Emission near the Hα Line. *The Astrophysical Journal Supplement Series*, *267*(1), 19. https://doi.org/10.3847/1538-4365/acd783

Ivezić, Ž., Connolly, A. J., VanderPlas, J. T., & Gray, A. (2014). *Statistics, data mining, and machine learning in astronomy: A Practical Python Guide for the Analysis of Survey Data*. Princeton University Press.

Jolliffe, I. T., & Cadima, J. (2016). Principal component analysis: a review and recent developments. *Philosophical Transactions of the Royal Society a Mathematical Physical and Engineering Sciences*, *374*(2065), 20150202. https://doi.org/10.1098/rsta.2015.0202

Kaspi, S., Maoz, D., Netzer, H., Peterson, B. M., Vestergaard, M., & Jannuzi, B. T. (2005). The Relationship between Luminosity and Broad-Line Region Size in Active Galactic Nuclei. *The Astrophysical Journal*, *629*(1), 61–71. https://doi.org/10.1086/431275

Kazantzidis, S., Mayer, L., Colpi, M., Madau, P., Debattista, V. P., Wadsley, J., Stadel, J., Quinn, T., & Moore, B. (2005). The fate of supermassive black holes and the evolution of the M_{BH}-σ relation in merging galaxies: the effect of gaseous dissipation. *The Astrophysical Journal*, *623*(2), L67–L70. https://doi.org/10.1086/430139

Kormendy, J., & Richstone, D. (1995). Inward Bound—The search for supermassive black holes in galactic nuclei. *Annual Review of Astronomy and Astrophysics*, *33*(1), 581–624. https://doi.org/10.1146/annurev.aa.33.090195.003053

Kovacević, A., Zeković, V., Ilić, D., Arbutina, B., Novaković, B., Onić, D., Marceta, D., & Djosović, V. (2022). Realization of the SUPERAST project. *Publications of Astronomical Society "Rudjer Bošković"*, *22*, 231-248. Bibcode: 2022PASRB..22..231K.

Krolik, J. H., Volonteri, M., Dubois, Y., & Devriendt, J. (2019). Population estimates for electromagnetically distinguishable supermassive binary black holes. *The Astrophysical Journal*, *879*(2), 110. https://doi.org/10.3847/1538-4357/ab24c9

Liu, X., Guo, H., Shen, Y., Greene, J. E., & Strauss, M. A. (2018). Hubble Space Telescope Wide Field Camera 3 Identifies an r_p = 1 Kpc Dual Active Galactic Nucleus in the Minor Galaxy Merger SDSS J0924+0510 at z = 0.1495. *The Astrophysical Journal*, *862*(1), 29. https://doi.org/10.3847/1538-4357/aac9cb

Lyke, B. W., Higley, A. N., McLane, J. N., Schurhammer, D. P., Myers, A. D., Ross, A. J., Dawson, K., Chabanier, S., Martini, P., Busca, N. G., Du Mas Des Bourboux, H., Salvato, M., Streblyanska, A., Zarrouk, P., Burtin, E., Anderson, S. F., Bautista, J., Bizyaev, D., Brandt, W. N., . . . Weaver, B. A. (2020). The Sloan Digital Sky Survey Quasar Catalog: Sixteenth Data Release. *The Astrophysical Journal Supplement Series*, *250*(1), 8. https://doi.org/10.3847/1538-4365/aba623

Mayer, L., Kazantzidis, S., Escala, A., & Callegari, S. (2010). Direct formation of supermassive black holes via multi-scale gas inflows in galaxy mergers. *Nature*, *466*(7310), 1082–1084. https://doi.org/10.1038/nature09294

Merrit, D. & Milosavljevic, M. (2005). Massive Black Hole Binary Evolution. *Living Reviews in Relativity, 8*(8), https://doi.org/10.48550/arXiv.astro-ph/0410364

Netzer, H. (2015). Revisiting the unified model of active galactic nuclei. *Annual Review of Astronomy and Astrophysics*, *53*(1), 365–408. https://doi.org/10.1146/annurev-astro-082214-122302

Nguyen, K., Bogdanović, T., Runnoe, J. C., Taylor, S. R., Sesana, A., Eracleous, M., & Sigurdsson, S. (2020). Pulsar timing array constraints on the merger timescale of subparsec supermassive black hole binary candidates. *The Astrophysical Journal Letters*, *900*(2), L42. https://doi.org/10.3847/2041-8213/abb2ab

Peterson, B. M. (2013). Measuring the masses of supermassive black holes. *Space Science Reviews*, *183*(1–4), 253–275. https://doi.org/10.1007/s11214-013-9987-4

Poindexter, S., Morgan, N., & Kochanek, C. S. (2008). The spatial structure of an accretion disk. *The Astrophysical Journal*, *673*(1), 34–38. https://doi.org/10.1086/524190

Popović, L. Č. (2012). Super-massive binary black holes and emission lines in active galactic nuclei. *New Astronomy Reviews*, *56*(2–3), 74–91. https://doi.org/10.1016/j.newar.2011.11.001

Popović, L. Č., Mediavilla, E., Bon, E., & Ilić, D. (2004). Contribution of the disk emission to the broad emission lines in AGNs: Two-component model. *Astronomy and Astrophysics*, *423*(3), 909–918. https://doi.org/10.1051/0004-6361:20034431

Popović, L. Č., Simić, S., Kovačević, A., & Ilić, D. (2021). Detecting subparsec supermassive binary black holes: Long-term monitoring perspective. *Monthly Notices of the Royal Astronomical Society*, *505*(4), 5192–5211. https://doi.org/10.1093/mnras/stab1510

Rakić, N. (2022). Kinematics of the H α and H β broad-line region in an SDSS sample of type-1 AGNs. *Monthly Notices of the Royal Astronomical Society*, *516*(2), 1624–1634. https://doi.org/10.1093/mnras/stac2259

Roos, N. (1981). Galaxy mergers and active galactic nuclei. *Astronomy and Astrophysics, vol. 104*(2)*, p. 218-228.* Bibcode: 1981A&A...104..218R

Savić, D., Marin, F., & Popović, L. Č. (2019). Predicting the broad-lines polarization emitted by supermassive binary black holes. *Astronomy and Astrophysics*, *623*, A56. https://doi.org/10.1051/0004-6361/201834443

Shakura, N. I. & Sunyaev, R. A. (1973). Black holes in binary systems. Observational appearance. *Astronomy and Astrophysics*, *24*, p. 337 – 355, Bibcode:1973A&A....24..337S.

Shemmer, O., Netzer, H., Maiolino, R., Oliva, E., Croom, S., Corbett, E., & Di Fabrizio, L. (2004). Near-Infrared spectroscopy of High-Redshift active galactic nuclei. I. A Metallicity–Accretion rate relationship. *The Astrophysical Journal*, *614*(2), 547–557. https://doi.org/10.1086/423607

Shlens, J. (2014). A tutorial on principal component analysis. *arXiv (Cornell University)*. https://doi.org/10.48550/arxiv.1404.1100

Simic, S., et al., (2024). [Manuscript in preparation]

Simić, S., Popović, L. Č., Kovačević, A., & Ilić, D. (2021). The broad emission line asymmetry in a low mass ratio of supermassive binary black holes on elliptical orbits. *Astronomische Nachrichten*, *343*(1–2). https://doi.org/10.1002/asna.20210073

Smee, S. A., Gunn, J. E., Uomoto, A., Roe, N., Schlegel, D., Rockosi, C. M., Carr, M. A., Leger, F., Dawson, K. S., Olmstead, M. D., Brinkmann, J., Owen, R., Barkhouser, R. H., Honscheid, K., Harding, P., Long, D., Lupton, R. H., Loomis, C., Anderson, L., . . . York, D. G. (2013). THE MULTI-OBJECT, FIBER-FED

SPECTROGRAPHS FOR THE SLOAN DIGITAL SKY SURVEY AND THE BARYON OSCILLATION SPECTROSCOPIC SURVEY. *The Astronomical Journal*, *146*(2), 32. https://doi.org/10.1088/0004-6256/146/2/32

Vanderplas, J. T., Connolly, A. J., Ivezić, Ž., & Gray, A. (2012). Introduction to astroML: Machine learning for astrophysics. In *Conference on Intelligent Data Understanding (CIDU)* (pp. 47–54). IEEE. https://doi.org/10.1109/CIDU.2012.6382200

Volonteri, M., Haardt, F., & Madau, P. (2003a). The assembly and merging history of supermassive black holes in hierarchical models of galaxy formation. *The Astrophysical Journal*, *582*(2), 559–573. https://doi.org/10.1086/344675

Volonteri, M., Madau, P., & Haardt, F. (2003b). The formation of galaxy stellar cores by the hierarchical merging of supermassive black holes. *The Astrophysical Journal*, *593*(2), 661–666. https://doi.org/10.1086/376722

Walker, S. A., Fabian, A. C., Russell, H. R., & Sanders, J. S. (2014). The effect of the quasar H1821+643 on the surrounding intracluster medium: revealing the underlying cooling flow. *Monthly Notices of the Royal Astronomical Society*, *442*(3), 2809–2816. https://doi.org/10.1093/mnras/stu1067

Wang, J. -M., Songsheng, Y. -Y., Li, Y. -R, & Du, P. (2022). Final stage of merging binaries of supermassive black holes: observational signatures. *Monthly Notices of the Royal Astronomical Society*, *518*(3), 3397–3406. https://doi.org/10.1093/mnras/stac3266Woo, J. -H., Bae, H. -J, Son, D., et al., 2016, "*The Prevalence of Gas Outflows in Type 2 AGNs*", in *The Astrophysical Journal*, *817*(2), http://doi.org/10.3847/0004-637X/817/2/108.

Wu, X. -B, Wang, R., Kong, M. Z., Liu, F. K., & Han, J. L. (2004). Black hole mass estimation using a relation between the BLR size and emission line luminosity of AGN. *Astronomy and Astrophysics*, *424*(3), 793–798. https://doi.org/10.1051/0004-6361:20035845

Zuo, W., Wu, X. -B., Fan, X., Green, R., Wang, R., & Bian, F. (2015). BLACK HOLE MASS ESTIMATES AND RAPID GROWTH OF SUPERMASSIVE BLACK HOLES IN LUMINOUS z∼ 3.5 QUASARS. *The Astrophysical Journal*, *799*(2), 189. https://doi.org/10.1088/0004-637x/799/2/189

Appendix A. Derivation of Error Propagation

Since errors affect how the spectra are filtered and fitted, an accurate error propagation is needed to obtain the accurate filter and fit. This appendix shows the derivation of error propagation used in this thesis.

A.1 Error Propagation of Linear Interpolation

Given two points with the errors in y-axis as $(x_1, y_1 \pm \sigma_{y1})$ and $(x_2, y_2 \pm \sigma_{y2})$. Assuming a linear function,

$$y = y_1 + \frac{y_2 - y_1}{x_2 - x_1}(x - x_1) \tag{A.1}$$

For a function $y = f(y_1, y_2)$, where y_1 and y_2 are independent variables, the following general equation for error propagation can be used:

$$\sigma_y = \sqrt{\left(\frac{\partial y}{\partial y_1}\sigma_{y1}\right)^2 + \left(\frac{\partial y}{\partial y_2}\sigma_{y2}\right)^2} \tag{A.2}$$

The partial derivative for y with respect to y_1 is as follows:

$$\frac{\partial y}{\partial y_1} = \frac{\partial}{\partial y_1}\left(y_1 + \left(\frac{y_2 - y_1}{x_2 - x_1}\right)(x - x_1)\right)$$

Evaluating the partial derivation,

$$\frac{\partial y}{\partial y_1} = \left(\frac{x_2 - x}{x_2 - x_1}\right)$$

Similarly with respect to y_2

$$\frac{\partial y}{\partial y_2} = \left(\frac{x - x_1}{x_2 - x_1}\right)$$

Plugging equation A.3 and A.4 to A.2 yields,

$$\sigma_y = \sqrt{\left(\frac{x_2 - x}{x_2 - x_1}\right)^2 \sigma_{y1}^2 + \left(\frac{x - x_1}{x_2 - x_1}\right)^2 \sigma_{y2}^2} \tag{A.3}$$

A.2 Error Propagation of Maximum Value Normalization

Maximum value normalization sets the maximum value of a data to be 1. Given a value to be normalized $y \pm \sigma_y$ and a maximum value of the data $y_{max} \pm \sigma_{y,max}$, the normalization follows the following formula:

$$y_{norm} = y / y_{max} \tag{A.4}$$

Using the multiplication error propagation:

$$\frac{\sigma_{y,norm}}{y_{norm}} = \sqrt{\left(\frac{\sigma_y}{y}\right)^2 + \left(\frac{\sigma_{y,max}}{y_{max}}\right)^2} \tag{A.5}$$

Appendix B. Effect of Scaling

As previously stated, `sklearn` suggests scaling the data before performing PCA process with the reason being so that the eigenspectra have a standard deviation of 1 and mean of 0. The argument for scaling from the documentation is to ease convergence and to give better performance on PCA. `sklearn` suggested `StandardScaler` procedure to perform the scaling. The `StandardScaler` procedure standardize features by removing mean and scaling to unit variance.

Figure B.1 shows the comparison of the first 5 eigenspectra generated scaled flux and unscaled flux. Figure 1 in Boroson & Lauer (2010) gives a sample of the first 4 eigenspectra within the wavelength range. Comparing the eigenspectra shown in figure B.1, it is evident that the eigenspectral generated by the scaled flux does not conform to previous literature. Although Francis et al. (1992) suggested that the effect of scaling is negligible, figure B.1 shows that the effect of scaling is significant, so much so that scaling distorts the shape of the spectra.

Francis et al. (1992) performed a scaling procedure that's similar to the `StandardScaler` procedure. Francis et al. (1992) opt to use the unscaled flux due to its simplicity and ease of interpretation. This serves as another reason for this thesis to use the unscaled flux instead of the scaled one.

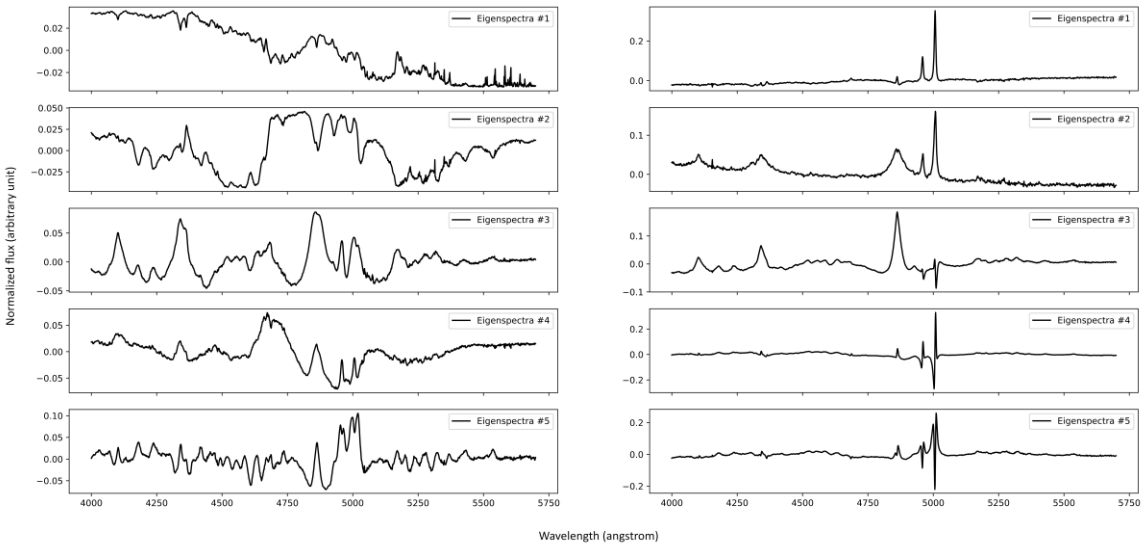

Figure B.1 Comparison of the first 5 eigenspectra generated by the scaled (*left*) and unscaled (*right*) flux.

Appendix C. Fitting Result of SDSS Spectra and Simulated Spectra of Very High Confidence SMBBH

C.1 Fitting result

This appendix presents the result of the spectra fitting, with the parameters of simulated spectra. Subsections are organized based on the classifications discussed in chapter 3. Additionally, components mass parameter M_i is presented in unit of $\log M_{\odot}$, component separation R is presented in the unit of parsec, and position is presented in the term of how long from the previous apocentric position (position 0% on figure IV.8).

C.1.1 Eracleous Objects

Out of 159 objects classified as Eracleous objects, 16.98% of objects have a high to very high confidence fitting. Some of the Eracleous objects are a duplicate of double-peaked objects that needed to be analyzed further. Figure C.1 shows 4 Eracleous objects with the best fit while the table below shows the fitting of all Eracleous objects.

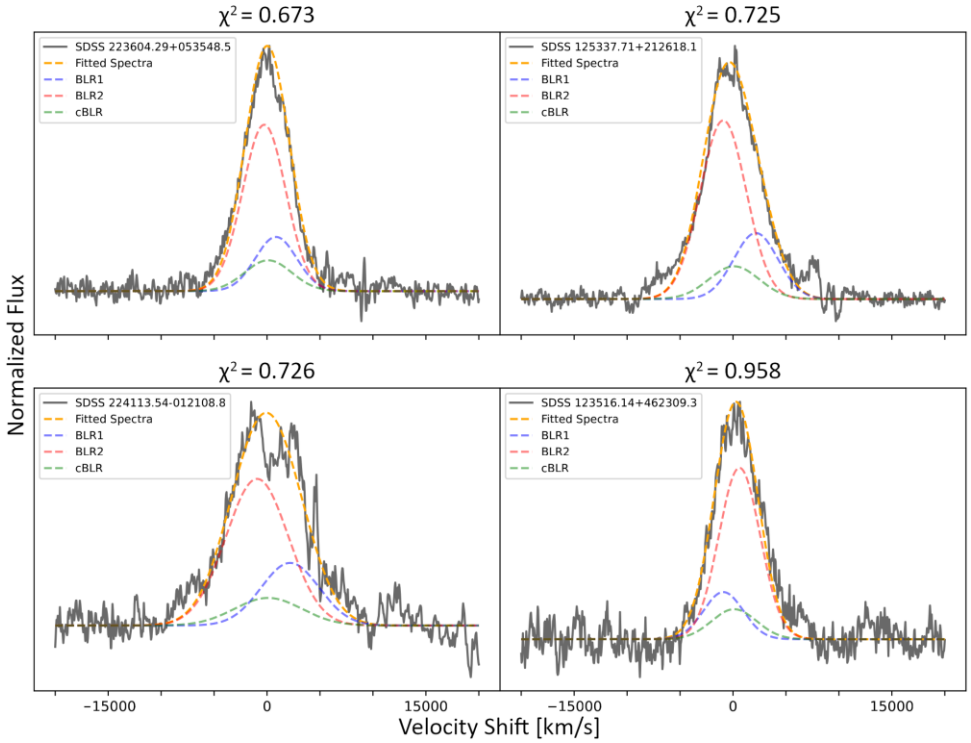

Figure C.1 Spectra of 4 Eracleous objects with the best fit, along with the fitted spectra.

SDSS designation	M_i ($\log M_\odot$)	Mass Ratio	R (pc)	Position (Year)	χ^2	Confidence
223604.29+053548.5	7	1:2	0.005	3.862	0.673	Very High
125337.71+212618.1	7	1:2	0.01	9.075	0.725	Very High
224113.54-012108.8	9	1:2	0.1	18.601	0.726	Very High
123516.14+462309.3	7	1:2	0.001	0.388	0.958	Very High
225307.36+194234.6	9	1:2	0.02	1.141	1.087	High
114803.18+565411.4	9	1:2	0.01	1.126	1.170	High
121114.56+365739.5	9	1:2	0.01	1.210	1.174	High
232932.17+043804.4	6	1:1	0.1	0.000	1.338	High
140700.40+282714.6	9	1:2	0.01	1.244	1.394	High
093728.57+324548.3	8	1:2	0.005	0.470	1.430	High
010312.99+022109.9	8	1:2	0.005	0.470	1.443	High
231821.08+322339.5	6	1:2	0.001	1.126	1.483	High
231101.69+182744.6	8	1:2	0.005	1.447	1.487	High
095048.38+392650.4	7	1:2	0.001	0.383	1.496	High
020840.66-062716.7	6	1:2	0.001	0.218	1.588	High
110436.33+212417.8	7	1:2	0.001	0.122	1.597	High
081501.85+525255.5	6	1:2	0.001	0.454	1.642	High
110539.81+342534.6	6	1:2	0.001	0.084	1.708	High
094859.47+433518.9	6	1:1	0.1	0.000	1.753	High
153934.80+473531.2	8	1:1	0.1	129.673	1.810	High
104013.47+383544.4	7	1:2	0.02	18.063	1.811	High
150527.60+294718.3	7	1:2	0.001	0.122	1.846	High
233908.79-000637.8	8	1:2	0.005	0.395	1.858	High
020354.68-060844.0	8	1:2	0.1	100.836	1.871	High
225448.43+261905.0	9	1:2	0.1	20.195	1.968	High
222704.35+022356.1	6	1:1	0.1	0.000	1.974	High
020412.45+224226.1	7	1:2	0.001	0.117	1.995	High
002444.11+003221.2	9	1:2	0.02	1.616	2.100	Low
080411.19+431640.6	6	1:2	0.001	0.908	2.101	Low
161911.24+501109.2	7	1:2	0.01	9.243	2.137	Low
222024.58+010931.3	7	1:1	0.01	14.614	2.153	Low
225639.16+261843.6	7	1:2	0.001	0.122	2.199	Low
150813.03+484710.7	7	1:2	0.01	4.033	2.207	Low
093653.84+533126.8	9	1:2	0.02	1.331	2.218	Low
135852.46+295413.1	9	1:2	0.1	32.419	2.235	Low
101707.63+095452.4	8	1:2	0.005	0.470	2.255	Low
162853.90+412322.4	8	1:2	0.1	97.475	2.260	Low
074007.27+410903.6	7	1:2	0.001	0.122	2.336	Low
023450.82-021711.8	7	1:2	0.001	0.383	2.382	Low
094755.99+535000.3	7	1:2	0.001	0.122	2.424	Low
113908.96+591154.7	6	1:1	0.1	0.000	2.428	Low
230720.15+055305.2	6	1:1	0.1	0.000	2.478	Low
234605.79+153204.4	7	1:2	0.001	0.149	2.486	Low
125543.36+350952.7	8	1:2	0.005	0.470	2.509	Low

SDSS designation	M_i ($\log M_\odot$)	Mass Ratio	R (pc)	Position (Year)	χ^2	Confidence
130753.92+064213.9	8	1:2	0.02	6.013	2.518	Low
152139.66+033729.2	9	1:2	0.1	38.796	2.553	Low
161649.42+415416.3	6	1:2	0.001	0.185	2.557	Low
075407.95+431610.6	9	1:2	0.01	0.437	2.583	Low
143603.56+375131.3	9	1:2	0.1	36.139	2.591	Low
123707.43+074024.7	9	1:2	0.1	32.419	2.626	Low
081931.20+334837.5	9	1:2	0.02	1.093	2.630	Low
074126.38+354702.6	8	1:2	0.005	0.470	2.658	Low
141116.72+194440.0	6	1:2	0.001	0.050	2.666	Low
113330.30+105223.3	9	1:2	0.02	1.616	2.738	Low
004046.16+185424.3	7	1:2	0.001	0.388	2.751	Low
004151.99+181617.3	6	1:1	0.1	0.000	2.789	Low
090514.48+415153.5	8	1:1	0.1	125.556	2.799	Low
232256.65+185816.5	6	1:1	0.1	0.000	2.800	Low
134548.50+114443.5	6	1:2	0.001	0.286	2.802	Low
015530.02-085704.0	9	1:2	0.1	12.223	2.802	Low
001340.44+040859.6	7	1:2	0.01	15.461	2.872	Low
002244.29-014550.9	9	1:2	0.01	0.504	2.872	Low
091956.11+560720.4	6	1:2	0.001	0.504	2.923	Low
105747.71+324706.3	7	1:2	0.01	15.293	2.925	Low
234123.16+252606.4	9	1:2	0.1	38.264	2.979	Low
073226.19+344952.1	9	1:2	0.02	1.569	3.014	Very Low
140251.19+263117.5	8	1:2	0.005	1.447	3.019	Very Low
075403.60+481428.0	9	1:2	0.02	3.090	3.064	Very Low
170056.01+243928.2	9	1:2	0.02	1.093	3.146	Very Low
162439.95+323918.9	8	1:1	0.1	129.673	3.161	Very Low
093255.45+284036.7	9	1:2	0.01	1.126	3.167	Very Low
003612.50+054951.8	7	1:2	0.02	10.458	3.177	Very Low
115504.07+034850.3	9	1:2	0.01	1.126	3.306	Very Low
010352.47+003739.7	7	1:2	0.001	0.122	3.319	Very Low
074906.50+451033.8	6	1:2	0.001	1.597	3.324	Very Low
123022.17+662154.6	7	1:1	0.01	15.026	3.346	Very Low
083726.95+312104.8	9	1:2	0.1	32.419	3.357	Very Low
012558.06+151813.7	6	1:2	0.001	0.084	3.378	Very Low
162219.43+475132.4	7	1:2	0.001	0.202	3.396	Very Low
011550.47+251536.7	7	1:2	0.001	0.441	3.399	Very Low
085053.12+445122.4	9	1:2	0.1	34.013	3.423	Very Low
083017.92+293923.9	9	1:2	0.1	32.950	3.433	Very Low
151443.06+365050.4	9	1:2	0.1	18.601	3.433	Very Low
000859.26+255305.2	9	1:2	0.02	1.616	3.473	Very Low
230155.55-010649.0	7	1:2	0.005	3.625	3.543	Very Low
094620.86+334746.9	8	1:2	0.005	0.470	3.655	Very Low
153636.22+044127.0	9	1:2	0.01	1.109	3.687	Very Low
002902.97+195710.1	6	1:2	0.001	0.739	3.688	Very Low

SDSS designation	M_i ($\log M_\odot$)	Mass Ratio	R (pc)	Position (Year)	χ^2	Confidence
133432.34+171146.9	9	1:2	0.1	19.132	3.702	Very Low
225607.53+194028.6	7	1:2	0.001	0.202	3.787	Very Low
214843.56+001054.5	8	1:2	0.02	6.163	3.814	Very Low
163746.50+114949.2	7	1:1	0.1	240.830	3.831	Very Low
225421.65+211816.2	9	1:2	0.01	1.126	3.848	Very Low
145224.67+452223.6	7	1:2	0.01	15.630	3.911	Very Low
083010.50+321352.7	7	1:2	0.001	0.377	3.923	Very Low
121740.80+493118.0	6	1:2	0.001	0.840	3.938	Very Low
010320.62+271937.4	6	1:1	0.1	0.000	3.956	Very Low
114559.55+461309.1	6	1:2	0.005	6.952	3.993	Very Low
231954.52+250247.3	6	1:1	0.1	0.000	3.999	Very Low
154019.56-020505.4	9	1:2	0.1	19.132	4.006	Very Low
022507.93-003532.9	9	1:2	0.01	1.109	4.013	Very Low
235802.64+092631.0	9	1:2	0.01	1.109	4.035	Very Low
113617.11+441022.5	7	1:2	0.005	1.842	4.071	Very Low
013521.27+062548.5	9	1:2	0.01	1.109	4.075	Very Low
012012.46+071258.2	8	1:2	0.005	1.447	4.091	Very Low
083109.39+143448.9	8	1:2	0.01	3.880	4.104	Very Low
142129.75+474724.5	8	1:2	0.005	0.470	4.109	Very Low
075057.26+353037.6	7	1:2	0.01	15.630	4.141	Very Low
000115.88+051902.0	8	1:2	0.1	122.684	4.264	Very Low
011304.63+350425.5	8	1:2	0.02	4.359	4.345	Very Low
030021.40-071458.8	9	1:2	0.01	1.210	4.386	Very Low
105444.70+483139.1	7	1:2	0.01	3.697	4.449	Very Low
123054.11+110011.2	7	1:2	0.02	29.471	4.521	Very Low
012447.76+320727.4	9	1:2	0.01	1.210	4.530	Very Low
081054.17+232145.4	9	1:1	0.1	18.876	4.548	Very Low
081443.40+435314.7	7	1:2	0.001	0.143	4.574	Very Low
005419.26+055734.0	8	1:2	0.01	1.488	4.681	Very Low
224239.20+011805.8	8	1:2	0.01	1.222	4.693	Very Low
102839.11+450009.4	7	1:2	0.001	0.340	4.695	Very Low
223456.08+200751.9	8	1:2	0.1	36.973	4.713	Very Low
123001.02+335901.3	8	1:2	0.02	6.163	4.723	Very Low
095539.82+453216.9	7	1:2	0.001	0.388	4.841	Very Low
004607.97+090720.9	7	1:2	0.001	0.191	4.885	Very Low
000710.01+005329.0	9	1:2	0.1	19.132	4.939	Very Low
093844.45+005715.7	7	1:2	0.001	0.324	4.995	Very Low
074125.22+333319.9	9	1:2	0.1	36.139	5.013	Very Low
213954.03+033256.9	8	1:2	0.005	1.353	5.016	Very Low
093844.45+005715.7	7	1:2	0.001	0.324	5.023	Very Low
155700.38+312020.1	9	1:1	0.1	46.213	5.052	Very Low
092226.53+162719.3	9	1:1	0.1	18.876	5.065	Very Low
130534.49+181932.8	7	1:2	0.001	0.122	5.141	Very Low
115758.72-002220.9	7	1:2	0.001	0.143	5.149	Very Low

SDSS designation	M_i ($\log M_\odot$)	Mass Ratio	R (pc)	Position (Year)	χ^2	Confidence
105157.23+375429.1	9	1:2	0.02	1.331	5.211	Very Low
153539.24+564406.4	8	1:2	0.1	38.654	5.227	Very Low
100642.58+412201.9	7	1:2	0.001	0.202	5.259	Very Low
221217.12+035040.5	7	1:2	0.001	0.122	5.331	Very Low
120442.10+275411.8	8	1:2	0.1	129.406	5.390	Very Low
102412.23-013348.4	7	1:2	0.001	0.202	5.444	Very Low
115554.41+445628.3	9	1:2	0.1	34.544	5.515	Very Low
160243.91+174503.9	7	1:2	0.001	0.191	5.568	Very Low
224826.97-005350.5	9	1:2	0.1	38.796	5.579	Very Low
120924.07+103612.0	9	1:2	0.02	1.331	5.649	Very Low
020002.14+021655.8	8	1:2	0.01	1.435	5.698	Very Low
091928.69+143202.6	9	1:2	0.01	1.109	5.775	Very Low
000549.49+102237.6	6	1:2	0.001	0.840	5.924	Very Low
010940.24+072446.4	6	1:2	0.001	0.034	5.939	Very Low
154342.46+461233.4	8	1:2	0.1	100.836	5.955	Very Low
115839.90+625427.9	9	1:2	0.01	1.227	6.050	Very Low
020002.14+012043.6	6	1:1	0.1	0.000	6.635	Very Low
163745.13+471733.8	7	1:2	0.001	0.122	7.043	Very Low
020429.17+031934.5	7	1:2	0.001	0.446	7.095	Very Low
121716.08+080942.0	8	1:2	0.005	1.259	7.199	Very Low
092116.12+383537.6	7	1:2	0.001	0.340	7.202	Very Low
080814.70+475244.7	8	1:2	0.01	3.242	7.213	Very Low
235409.17-001947.9	8	1:2	0.01	3.189	8.173	Very Low
213004.76-010244.4	8	1:2	0.01	3.189	8.506	Very Low
161826.93+081950.7	9	1:2	0.02	1.474	10.210	Very Low
011226.53+050429.0	8	1:2	0.01	3.826	17.402	Very Low
230614.18-010024.4	7	1:2	0.001	0.340	17.499	Very Low

C.1.2 Double-peaked objects

Out of 29 objects with double-peaked broad Hβ spectra, which includes the duplicate objects, only 13.8% of objects have a high to very high confidence fitting. These objects need further scrutiny as due to further subtraction, the double peaks are not properly reconstructed. Figure C.2 shows 4 double-peaked objects with the best fit while the table below shows the fitting of all double-peaked objects.

SDSS designation	M_i ($\log M_\odot$)	Mass Ratio	R (pc)	Position (Year)	χ^2	confidence
222435.29-001103.9	6	1:2	0.001	0.084	0.468	Very High
224113.54-012108.8	9	1:2	0.1	33.481	0.615	Very High
125157.90+061341.6	6	1:2	0.001	0.588	0.897	Very High
225307.36+194234.6	9	1:2	0.02	1.141	1.146	High
080411.19+431640.6	6	1:2	0.001	0.908	2.187	Low
094755.99+535000.3	7	1:2	0.001	0.122	2.221	Low
093943.75+560230.5	6	1:2	0.001	1.092	2.301	Low
230720.15+055305.2	6	1:1	0.1	0.000	2.572	Low

SDSS designation	M_i ($\log M_\odot$)	Mass Ratio	R (pc)	Position (Year)	χ^2	confidence
002244.29-014550.9	9	1:2	0.01	0.504	2.744	Low
235321.28-015314.2	6	1:2	0.001	0.202	3.087	Very Low
011910.02+013127.9	9	1:2	0.01	1.126	3.262	Very Low
012558.06+151813.7	6	1:2	0.001	0.101	3.307	Very Low
011550.47+251536.7	7	1:2	0.001	0.441	3.334	Very Low
074906.50+451033.8	6	1:2	0.001	0.118	3.379	Very Low
170717.75+453610.5	6	1:2	0.001	0.050	3.423	Very Low
133432.34+171146.9	9	1:2	0.1	19.132	3.509	Very Low
153636.22+044127.0	9	1:2	0.01	1.109	3.705	Very Low
111754.31+263416.6	6	1:1	0.1	0.000	3.842	Very Low
145224.67+452223.6	7	1:2	0.01	15.630	3.843	Very Low
222428.53+261423.2	6	1:1	0.1	514.576	4.117	Very Low
152526.46+450651.7	7	1:2	0.001	0.335	4.330	Very Low
081443.40+435314.7	7	1:2	0.001	0.143	4.709	Very Low
102839.11+450009.4	7	1:2	0.001	0.340	4.828	Very Low
020429.17+031934.5	8	1:2	0.005	0.395	5.887	Very Low
084716.03+373218.0	6	1:1	0.1	0.000	5.980	Very Low
010940.24+072446.4	6	1:2	0.001	0.034	6.042	Very Low
092116.12+383537.6	7	1:2	0.001	0.340	7.351	Very Low
013521.27+062548.5	9	1:2	0.01	1.109	8.121	Very Low
235409.17-001947.9	8	1:2	0.01	3.189	8.453	Very Low

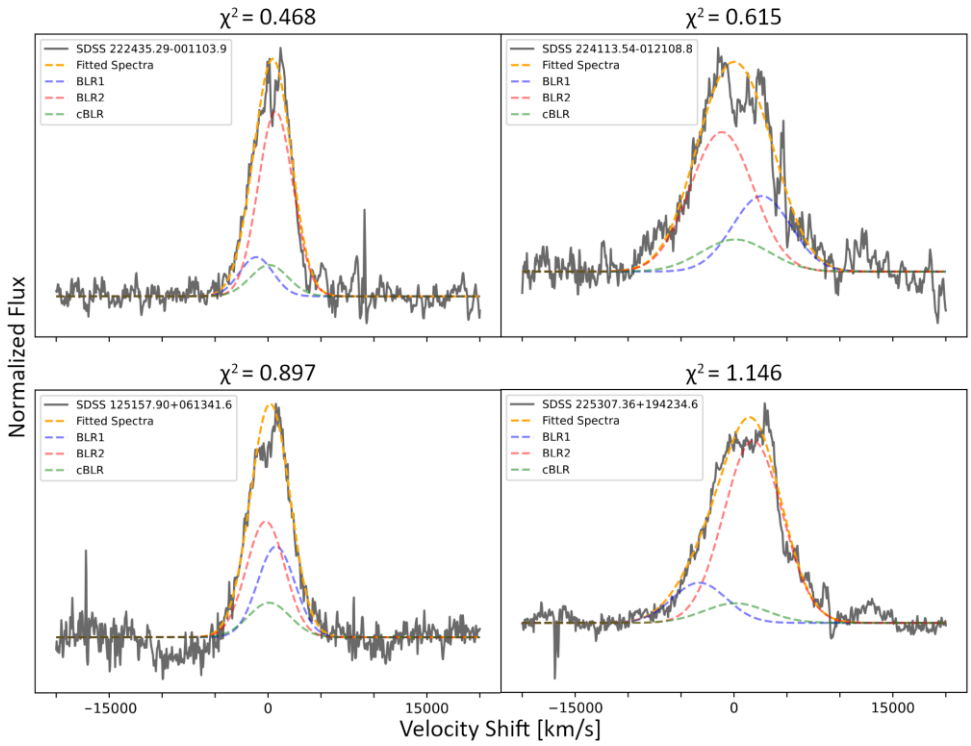

Figure C.2 Spectra of 4 double-peaked objects with the best fit, along with the fitted spectra.

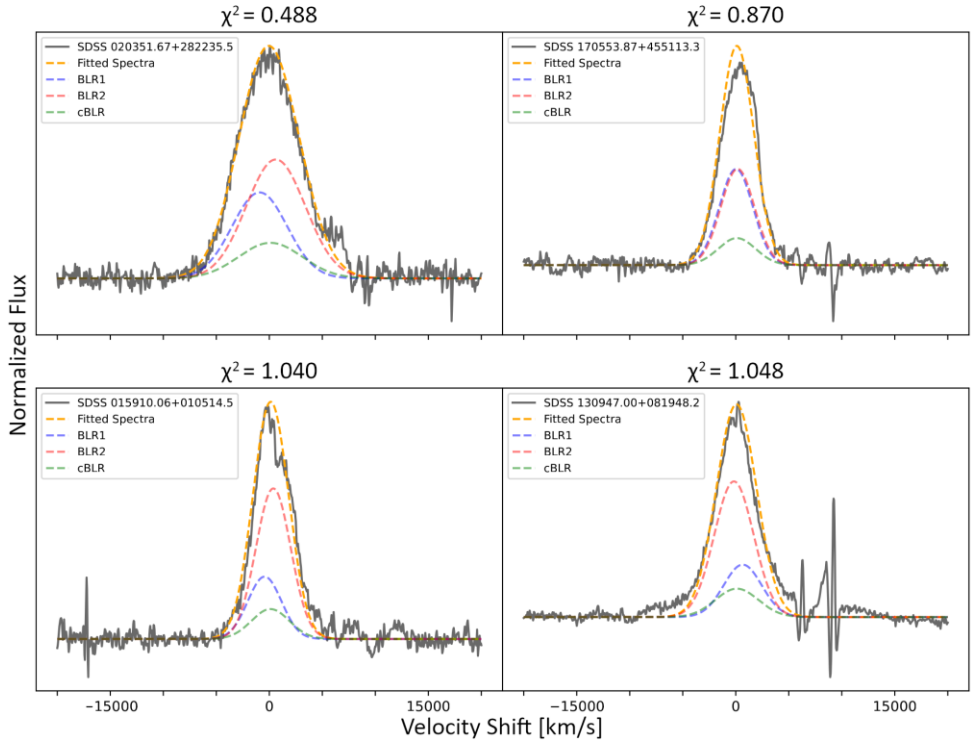

Figure C.3 Spectra of 4 asymmetric objects with the best fit, along with the fitted spectra.

C.1.3 Asymmetric objects

Out of 75 objects with asymmetric spectra, 20% of objects have a high to very high confidence fitting. Bad fits due for these objects might be caused by the positional configuration limitation when generating the spectra. Figure C.3 shows 4 objects with asymmetric broad Hβ spectra with the best fit while the table below shows the fitting of all asymmetric objects.

SDSS designation	M_i ($\log M_\odot$)	Mass Ratio	R (pc)	Position (Year)	χ^2	confidence
020351.67+282235.5	9	1:2	0.1	38.796	0.488	Very High
170553.87+455113.3	6	1:1	0.1	0.000	0.870	Very High
015910.06+010514.5	6	1:2	0.005	0.752	1.040	High
130947.00+081948.2	6	1:2	0.005	7.328	1.048	High
092809.43+383000.5	8	1:2	0.005	0.470	1.170	High
004256.97+333601.6	6	1:1	0.1	535.159	1.200	High
081652.24+425829.3	6	1:1	0.1	0.000	1.307	High
073309.20+455506.2	6	1:1	0.1	0.000	1.315	High
011808.82+195036.1	7	1:2	0.01	15.966	1.408	High
092313.69+372656.6	9	1:2	0.1	12.755	1.413	High
234440.02-003231.6	6	1:1	0.1	514.576	1.502	High
074455.95+364743.8	6	1:2	0.001	0.168	1.802	High
230524.41+284846.8	8	1:2	0.01	1.329	1.825	High
161425.17+375210.7	7	1:2	0.001	0.122	1.877	High
103440.91+443105.0	7	1:2	0.001	0.122	1.982	High

SDSS designation	M_i ($\log M_\odot$)	Mass Ratio	R (pc)	Position (Year)	χ^2	confidence
082802.14+514930.6	6	1:1	0.005	6.213	2.036	Low
101326.90+355806.8	7	1:2	0.001	0.143	2.170	Low
015025.35+091450.9	6	1:1	0.1	0.000	2.222	Low
092703.19+522316.4	7	1:2	0.1	0.000	2.230	Low
082658.56+190921.5	7	1:2	0.001	0.340	2.299	Low
010205.89+001156.9	8	1:2	0.005	1.428	2.340	Low
080852.25+131908.7	7	1:2	0.02	28.045	2.360	Low
121619.40+213351.0	6	1:2	0.01	0.531	2.393	Low
224927.48-025243.5	9	1:2	0.01	0.504	2.407	Low
021657.78-032459.4	6	1:1	0.1	0.000	2.489	Low
141920.30+051109.2	7	1:2	0.001	0.388	2.537	Low
155207.17+525347.1	6	1:2	0.001	0.151	2.578	Low
091955.34+552137.1	6	1:2	0.001	1.092	2.587	Low
222709.91+315226.6	9	1:2	0.01	1.126	2.715	Low
081651.10+180249.6	6	1:2	0.001	0.034	2.806	Low
231517.07+182814.5	6	1:1	0.1	0.000	2.842	Low
100003.72+313145.7	6	1:1	0.1	411.660	2.846	Low
160732.86+484619.9	6	1:1	0.1	843.904	2.855	Low
113706.84+013947.9	7	1:2	0.001	0.329	2.880	Low
224231.83+240930.2	9	1:2	0.01	1.126	2.892	Low
133636.65+420934.1	8	1:2	0.1	33.612	2.968	Low
101719.02+151620.8	7	1:2	0.001	0.335	3.020	Very Low
002933.96+323802.5	8	1:2	0.02	6.163	3.053	Very Low
092703.01+390220.8	7	1:2	0.001	0.446	3.207	Very Low
023922.87-000119.6	6	1:1	0.1	0.000	3.244	Very Low
110411.40+223946.7	6	1:2	0.001	0.050	3.265	Very Low
074756.99+454527.7	7	1:2	0.01	4.201	3.278	Very Low
135335.92+263147.5	9	1:2	0.1	33.481	3.314	Very Low
222749.21+000042.9	6	1:1	0.1	493.993	3.354	Very Low
021322.56-054100.3	6	1:2	0.001	0.218	3.542	Very Low
232202.60+211356.5	9	1:2	0.02	3.185	3.554	Very Low
074948.26+345444.0	6	1:1	0.1	0.000	3.589	Very Low
153102.48+435637.6	6	1:1	0.1	0.000	3.632	Very Low
164258.80+394837.0	6	1:2	0.001	0.034	3.709	Very Low
232000.48+222001.7	8	1:2	0.02	10.071	3.733	Very Low
082219.50+340044.9	7	1:2	0.001	0.388	3.780	Very Low
143204.60+394439.0	9	1:2	0.01	1.210	3.861	Very Low
122503.37+293931.0	6	1:2	0.001	0.050	3.932	Very Low
222428.53+261423.2	6	1:1	0.1	535.159	3.966	Very Low
010002.32+001642.4	6	1:2	0.001	0.992	3.996	Very Low
232245.78+074958.1	8	1:2	0.02	10.823	4.065	Very Low
220225.61+282821.2	9	1:2	0.1	18.069	4.122	Very Low
154833.02+442226.0	7	1:2	0.005	3.862	4.166	Very Low
152526.46+450651.7	7	1:2	0.001	0.335	4.267	Very Low

SDSS designation	M_i ($\log M_\odot$)	Mass Ratio	R (pc)	Position (Year)	χ^2	confidence
000729.30+061916.7	8	1:1	0.1	146.139	4.303	Very Low
003947.82-021204.9	7	1:2	0.01	3.865	4.311	Very Low
082438.99+405707.7	7	1:2	0.01	15.461	4.353	Very Low
114421.47+432206.0	8	1:2	0.1	97.475	4.466	Very Low
014017.06-005003.0	8	1:2	0.01	3.880	4.613	Very Low
015555.33+040620.3	8	1:2	0.1	124.364	4.663	Very Low
140658.70+144238.3	7	1:1	0.005	2.401	4.758	Very Low
235321.62-002840.6	7	1:2	0.001	0.340	4.790	Very Low
092837.98+602521.0	7	1:2	0.005	2.674	4.873	Very Low
105151.44-005117.6	9	1:1	0.1	18.876	5.067	Very Low
002419.09-013817.5	6	1:1	0.1	0.000	5.090	Very Low
091542.24+251939.0	7	1:2	0.001	0.202	5.302	Very Low
150455.56+564920.3	8	1:2	0.005	0.470	5.365	Very Low
123325.78+093123.3	9	1:1	0.02	4.075	6.204	Very Low
222912.08+312410.1	7	1:2	0.01	4.033	6.851	Very Low
225452.22+004631.3	6	1:1	0.1	0.000	9.275	Very Low

C.1.4 Broad objects

Out of 31 objects with very broad Hβ spectra, 35.5% of objects have a high to very high confidence fitting. These objects might be a good candidate to test the improvement to include the two-component model for the spectra simulation. Figure C.4 shows 4 broad objects with the best fit while the table below shows the fitting of all broad objects.

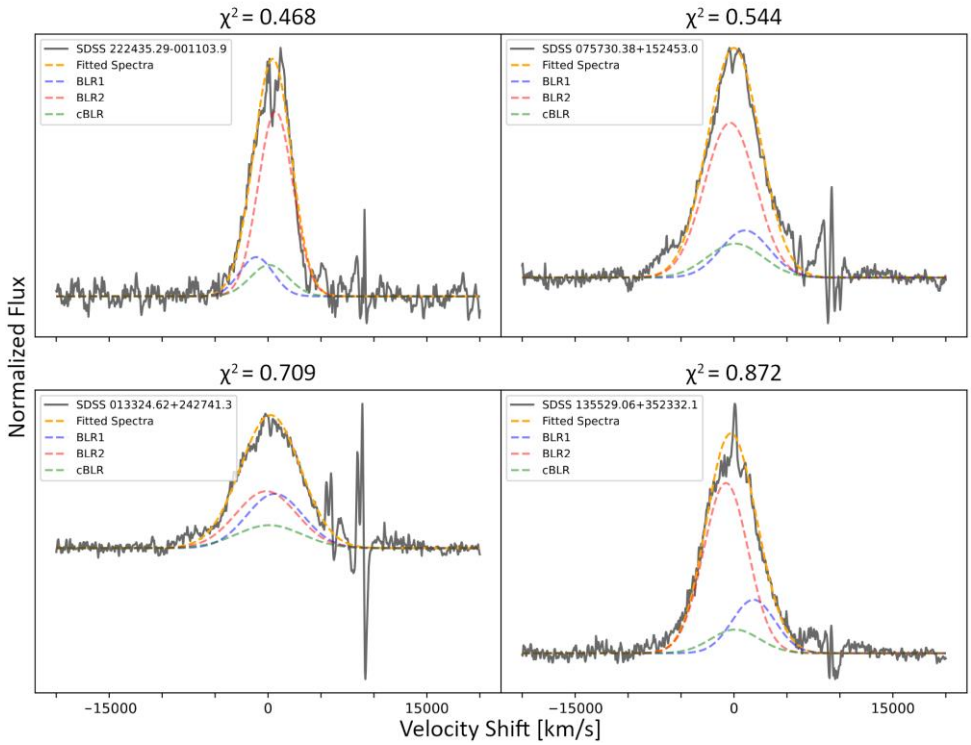

Figure C.4 Spectra of 4 broad objects with the best fit, along with the fitted spectra.

SDSS designation	M_i ($\log M_\odot$)	Mass Ratio	R (pc)	Position (Year)	χ^2	confidence
222435.29-001103.9	6	1:2	0.001	0.084	0.468	Very High
075730.38+152453.0	8	1:2	0.1	104.197	0.544	Very High
013324.62+242741.3	9	1:2	0.01	0.504	0.709	Very High
135529.06+352332.1	7	1:2	0.005	3.565	0.872	Very High
012648.09+032706.7	6	1:2	0.001	0.101	1.096	High
093527.09+261709.6	6	1:1	0.1	288.162	1.241	High
234955.70+302940.1	9	1:2	0.02	1.283	1.355	High
121037.56+315706.0	7	1:2	0.1	260.411	1.474	High
020441.90+022408.8	6	1:1	0.1	0.000	1.585	High
124139.72+493405.4	9	1:2	0.1	12.755	1.598	High
134231.22+382903.3	6	1:1	0.1	411.660	1.998	High
152757.67+223304.0	6	1:1	0.1	0.000	2.050	Low
235439.14+005751.9	9	1:2	0.1	15.412	2.080	Low
224817.51-101547.1	8	1:1	0.1	127.615	2.112	Low
093943.75+560230.5	6	1:2	0.001	1.092	2.380	Low
144701.77+323411.7	8	1:2	0.005	1.353	2.784	Low
014302.55+222610.7	7	1:2	0.005	2.020	3.039	Very Low
231240.03-083919.8	6	1:2	0.02	12.025	3.078	Very Low
011910.02+013127.9	9	1:2	0.01	1.126	3.548	Very Low
162021.81+173623.9	9	1:2	0.1	34.013	3.866	Very Low
011956.16+302102.0	8	1:2	0.01	3.614	3.978	Very Low
134737.45+301252.2	9	1:1	0.1	18.876	3.983	Very Low
002831.71-000413.2	7	1:2	0.005	3.743	4.352	Very Low
025231.19+034112.7	9	1:2	0.02	1.093	4.368	Very Low
004520.17-034842.9	9	1:2	0.1	36.139	4.516	Very Low
032213.89+005513.4	6	1:1	0.1	0.000	4.530	Very Low
224102.02+273259.4	9	1:2	0.02	3.185	4.639	Very Low
080452.73+212050.2	9	1:2	0.02	1.331	4.983	Very Low
171448.50+332738.3	7	1:2	0.001	0.388	5.063	Very Low
094715.56+631716.4	9	1:2	0.01	0.504	5.090	Very Low
082405.19+445246.0	6	1:1	0.1	0.000	11.825	Very Low

C.2 Simulated spectra of objects with very high confidence

This section shows the simulated spectra during certain positional configurations throughout observation time of SMBBH with certain mass and separation configurations. Figure C.5 to C.12 shows 10 variations of broad Hβ spectra in 1 period revolution of SMBBH with specified parameters.

The mass and separation configurations chosen are the from the objects with "*very high"* confidence fitting. The mass-separation configurations are shown in the table below, along with the object that fitted to the mass-separation parameters with high confidence:

SDSS Designation	Object Classification	M_i ($\log M_\odot$)	Mass Ratio	R (pc)	Time Variation Figure
170553.87+455113.3	Asymmetry	6	1:1	0.1	Figure C.5
222435.29-001103.9	Broad Double Peaked	6	1:2	0.001	Figure C.6
125157.90+061341.6	Double Peaked				
123516.14+462309.3	Eracleous	7	1:2	0.001	Figure C.7
223604.29+053548.5	Eracleous	7	1:2	0.005	Figure C.8
135529.06+352332.1	Broad				
125337.71+212618.1	Eracleous	7	1:2	0.01	Figure C.9
075730.38+152453.0	Broad	8	1:2	0.1	Figure C.10
013324.62+242741.3	Broad	9	1:2	0.01	Figure C.11
224113.54-012108.8	Eracleous Double Peaked	9	1:2	0.1	Figure C.12
020351.67+282235.5	Asymmetric				

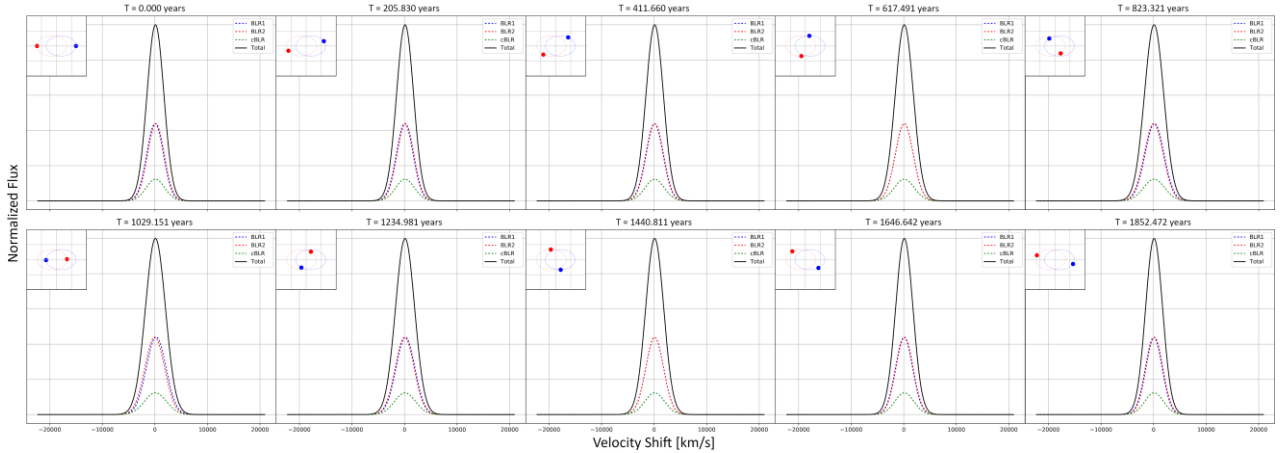

Figure C.5 Simulated spectra of SMBBH with configuration $M_i = 10^6\ M_\odot$, 1:1 ratio, and $R = 0.1\ pc$ focused on Hβ wavelength at $\lambda_{H\beta} = 4861$ Å. The blue and red circles on the top left of each graph shows the SMBBH configuration that emits the simulated spectra. Each of the SMBBH component emits the spectra with corresponding colour, and the black spectra lines show the observed total spectra.

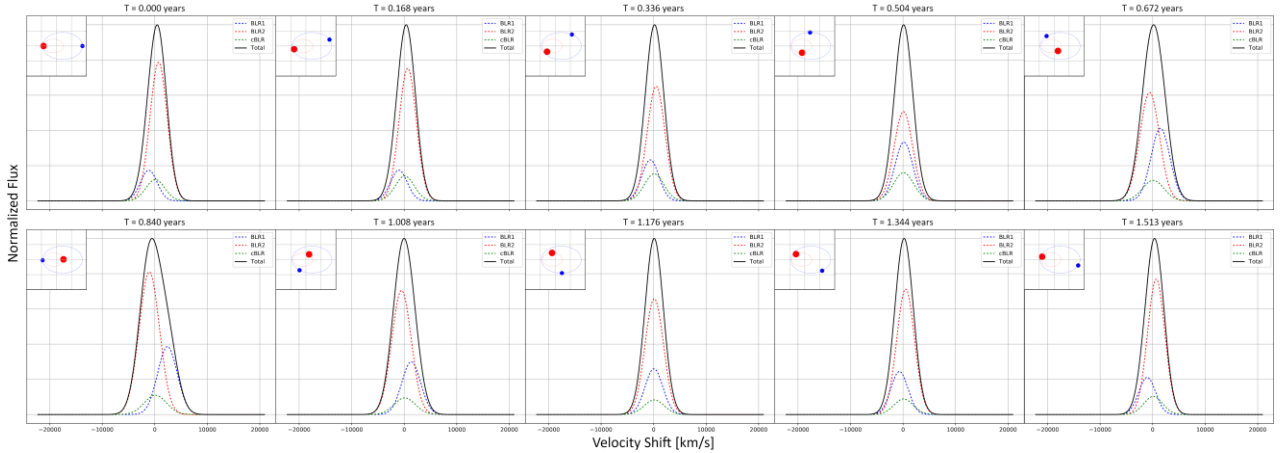

Figure C.6 The same as figure C.5 but with SMBBH configuration of $M_i = 10^6\ M_\odot$, 1:2 ratio, and $R = 0.001\ pc$.

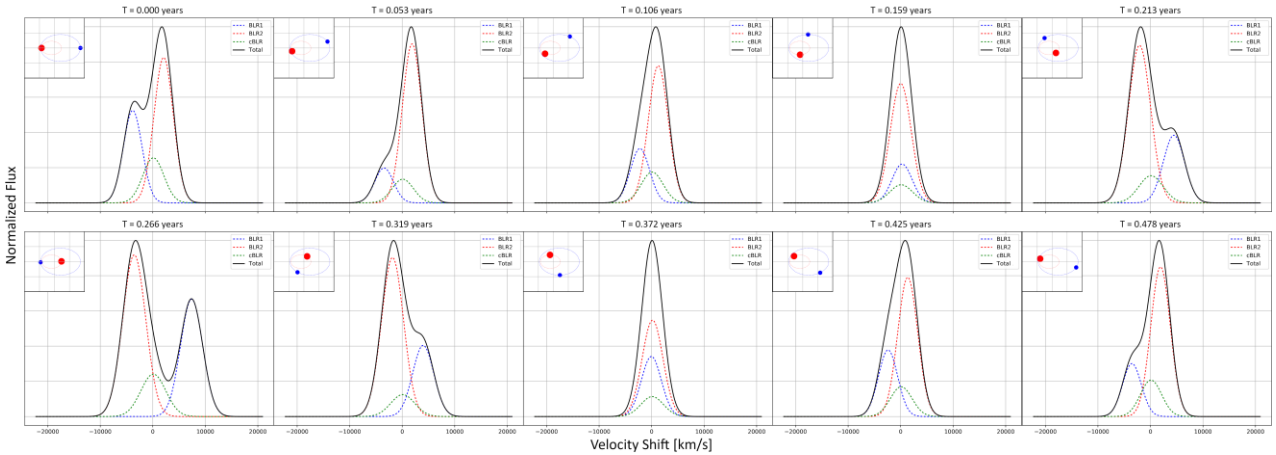

Figure C.7 The same as figure C.5 but with SMBBH configuration of $M_i = 10^7\ M_\odot$, 1:2 ratio, and $R = 0.001\ pc$.

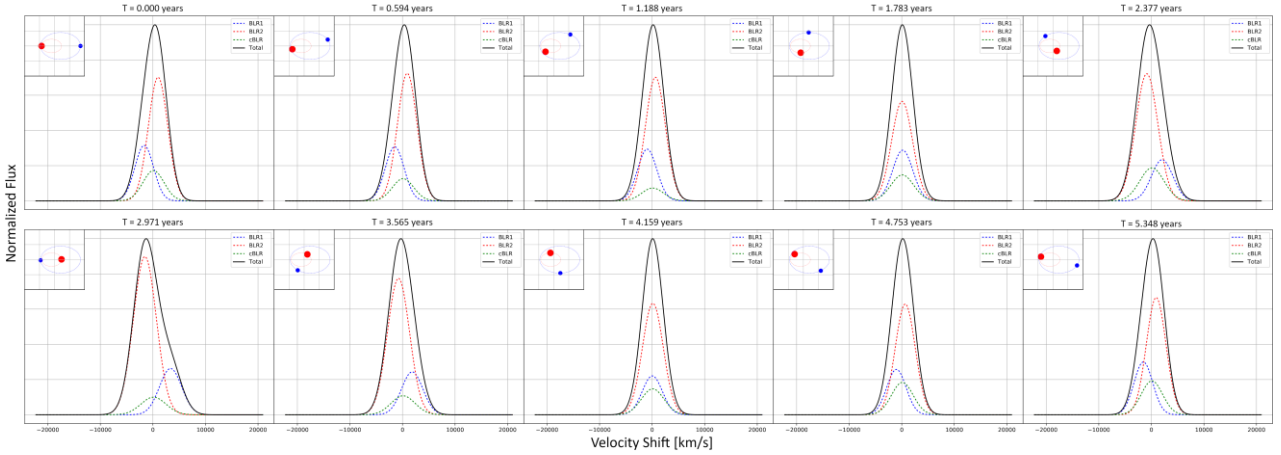

Figure C.8 The same as figure C.5 but with SMBBH configuration of $M_i = 10^7\ M_\odot$, 1:2 ratio, and $R = 0.005\ pc$.

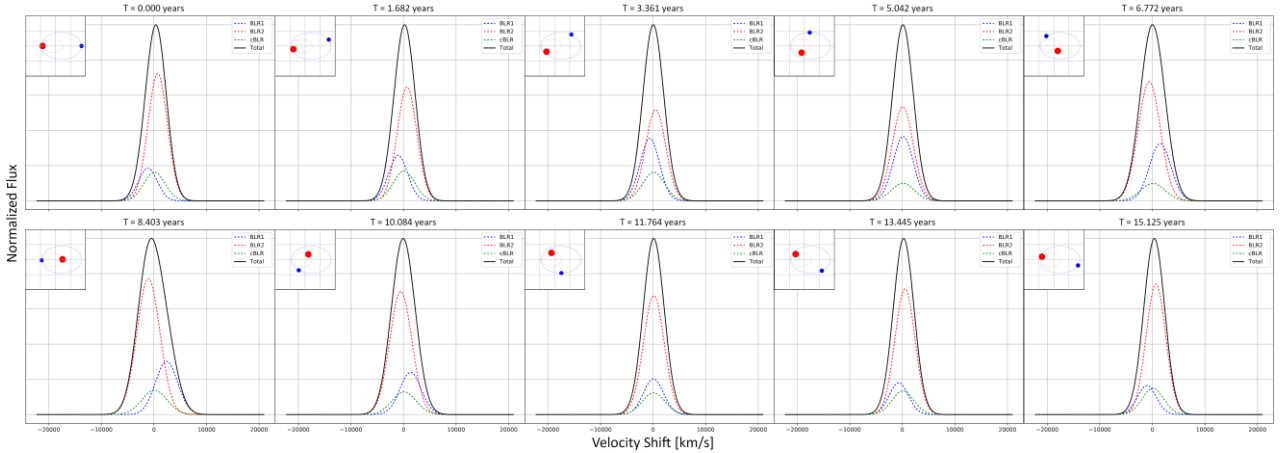

Figure C.9 The same as figure C.5 but with SMBBH configuration of $M_i = 10^7\ M_\odot$, 1:2 ratio, and $R = 0.01\ pc$.

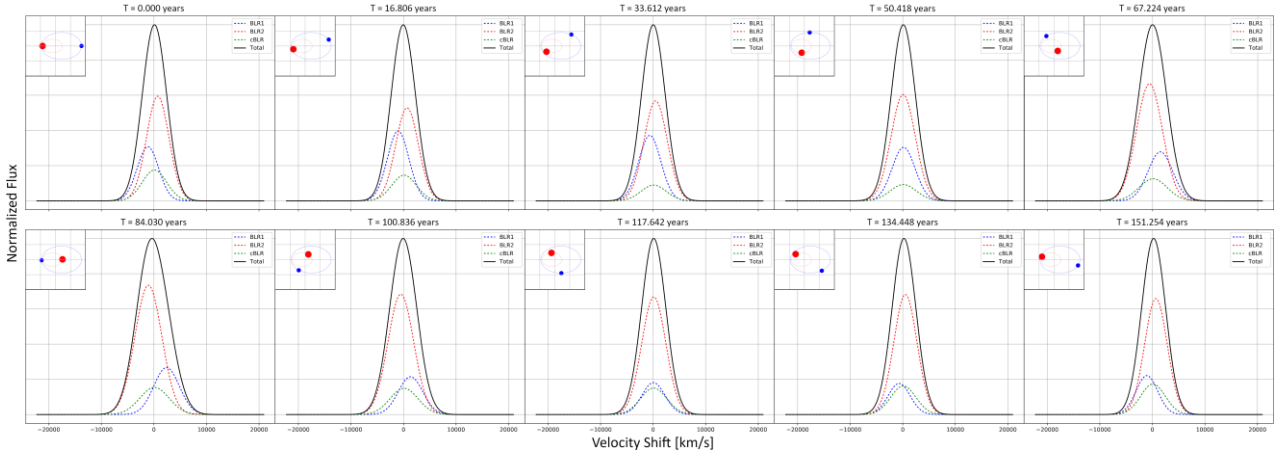

Figure C.10 The same as figure C.5 but with SMBBH configuration of $M_i = 10^8\ M_\odot$, 1:2 ratio, and $R = 0.1\ pc$.

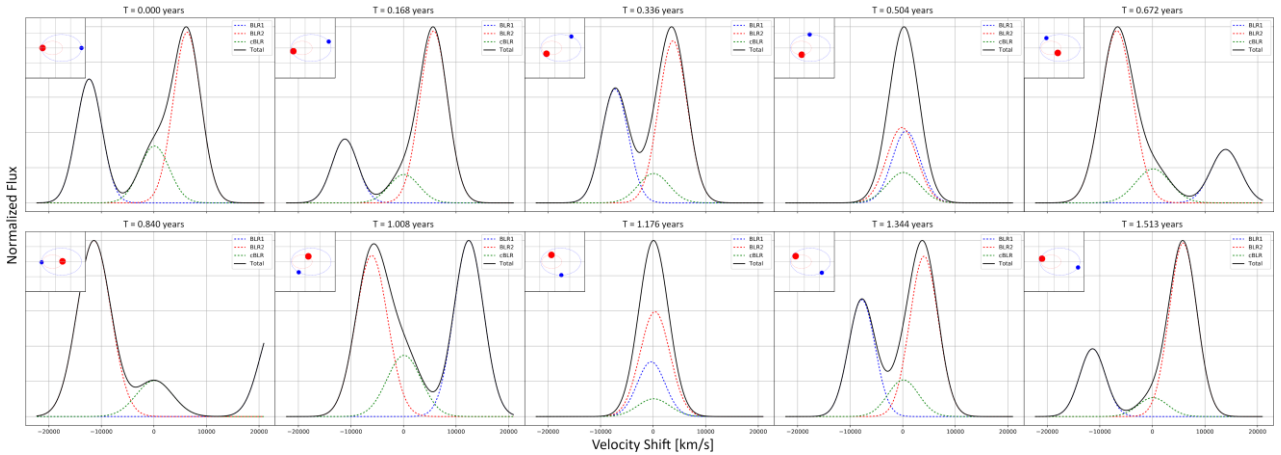

Figure C.11 The same as figure C.5 but with SMBBH configuration of $M_i = 10^9\ M_\odot$, 1:2 ratio, and $R = 0.01\ pc$.

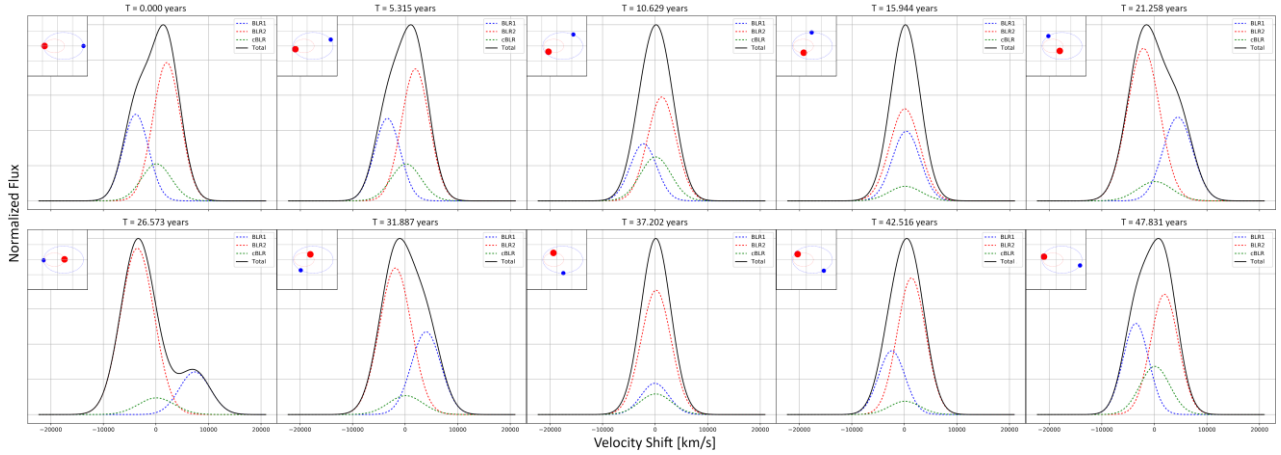

Figure C.12 The same as figure C.5 but with SMBBH configuration of $M_i = 10^9\ M_\odot$, 1:2 ratio, and $R = 0.1\ pc$.

Acknowledgement

There are several parties who helped and supported me in writing this thesis through various means, both directly and indirectly. Here, the writer would like to acknowledge their contributions in the writing of this thesis.

I would like to express my first gratitude to my supervisors, Luka Č. Popović, Francesco Tombesi, and Dragana Ilić for the support and guidance throughout this thesis, from my internship project that is included in the object selection phase to the thesis. In addition, I would like to also express my gratitude for Saša Simić for providing the code for the simulation, and the guidance for the modifications needed in the simulation, and to Anđjelka Kovačević for being my thesis committee.

Secondly, I extend my gratitude to Michael Eracleous, Todd A. Boroson, and their team for their prior research on SMBBH search using the PCA method which serves as the basis for the SMBBH search in this thesis. I would like to express people responsible for providing the SDSS data, especially Brad W. Lyke and team for the SDSS DR16 QSO catalogue. I am also thankful for Jake Vanderplas and the people responsible for AstroML for making the graphing source code, which is adapted to perform the spectra reconstruction, open for public. I would also like to acknowledge my use of the SuperAST computational cluster of the University of Belgrade's Astronomy Department, under the Faculty of Mathematics.

Thirdly, I would like to further extend my gratitude to other parties who helped and supported me during my master studies as a MASS student. I would like to thank my families back in Indonesia, especially my parents and sister, and my friends back home for their constant support, the Indonesian student's association in Rome, Nice, and Belgrade for giving me the feeling of home abroad, my fellow MASS students, especially the 1st edition students, for the time we spend together, the people responsible for MASS for providing me with this opportunity, and finally, the new friends I made along my study.

Author Biography

Aurellio Deandra (Jakarta, May 9th, 1999) started his higher education career at Bandung Institute of Technology (*Institut Teknologi Bandung*) in Bandung, Indonesia. He finished study with a Bachelor of Science degree in Astronomy major. His undergraduate research topic, which became his undergraduate thesis topic, was sonification and its application in astronomy, especially for accessibility and public outreach. This topic became his current main research interest, expanding to sonification application as an extension of data analysis and presentation, with the main philosophy of perceiving astronomy through different senses and perspectives. Currently, he is enrolled in MASS (Masters of Astrophysics and Space Science) which is part of Erasmus Mundus Joint Master program. His master's research focuses on spectroscopic analysis of active galactic nuclei.

Aurellio Deandra acknowledges support through an “Erasmus Mundus Joint Master (EMJM)” scholarship funded by the Euro-pean Union in the framework of the Erasmus+, Erasmus Mundus Joint Master in Astrophysics and Space Science – MASS. Views and opinions expressed are however those of the author(s) only and do not necessarily reflect those of the European Union or granting authority European Education and Culture Executive Agency (EACEA). Neither the European Union nor the granting authority can be held responsible for them.